

Left-invariant evolutions of wavelet transforms on the Similitude Group

Upanshu Sharma and Remco Duits

February 15, 2022

Abstract

Enhancement of multiple-scale elongated structures in noisy image data is relevant for many biomedical applications but commonly used PDE-based enhancement techniques often fail at crossings in an image. To get an overview of how an image is composed of local multiple-scale elongated structures we construct a multiple scale orientation score, which is a continuous wavelet transform on the similitude group, $SIM(2)$. Our unitary transform maps the space of images onto a reproducing kernel space defined on $SIM(2)$, allowing us to robustly relate Euclidean (and scaling) invariant operators on images to left-invariant operators on the corresponding continuous wavelet transform. Rather than often used wavelet (soft-)thresholding techniques, we employ the group structure in the wavelet domain to arrive at left-invariant evolutions and flows (diffusion), for contextual crossing preserving enhancement of multiple scale elongated structures in noisy images. We present experiments that display benefits of our work compared to recent PDE techniques acting directly on the images and to our previous work on left-invariant diffusions on orientation scores defined on Euclidean motion group.

Keywords: Continuous wavelet transform, Left-invariant vector fields, Similitude group, Orientation scores, Evolution equations, Diffusions on Lie groups, Medical imaging

1 Introduction

Elongated structures in the human body such as fibres and blood vessels often require analysis for diagnostic purposes. A wide variety of medical imaging techniques such as magnetic resonance imaging (MRI), microscopy, X-ray fluoroscopy, fundus imaging etc. exist to achieve this. Many (bio)medical questions related to such images require detection and tracking of the elongated structures present therein. Due to the desire to reduce acquisition time and radiation dosage the acquired medical images are often noisy, of low contrast and suffer from occlusions and incomplete data. Furthermore multiple-scale elongated structures exhibit crossings and bifurcations which is a notorious problem in (medical) imaging. Hence crossing-preserving enhancement of these structures is an important preprocessing step for subsequent detection.

In recent years PDE based techniques have gained popularity in the field of image processing. Due to well posed mathematical results these techniques lend themselves to stable algorithms and also allow mathematical and geometrical interpretation of classical methods such as Gaussian and morphological filtering, dilation or erosion etc. on \mathbb{R}^d . These techniques typically regard the original image, $f \in \mathbb{R}^2 \rightarrow \mathbb{R}$, as an initial state of a parabolic (diffusion like) evolution process yielding filtered versions, $u_f : \mathbb{R}^2 \times \mathbb{R}^+ \rightarrow \mathbb{R}$. Here u_f is called the scale space representation of image f . The domain of u_f is scale space $\mathbb{R}^2 \times \mathbb{R}^+$. A typical scale space evolution is of the form

$$\begin{cases} \partial_s u_f(\mathbf{x}, s) &= \nabla_{\mathbf{x}} \cdot (C(u_f(\cdot, s))(\mathbf{x}) \nabla_{\mathbf{x}} u_f)(\mathbf{x}, s) \\ u_f(\mathbf{x}, 0) &= f(\mathbf{x}), \end{cases} \quad (1)$$

where $C(u_f(\cdot, s))(\mathbf{x})$ models the diffusivity depending on the differential structure at $(\mathbf{x}, s, u_f(\mathbf{x}, s)) \in \mathbb{R}^d \times \mathbb{R}^+ \times \mathbb{R}$. For $C = 1$, Eq.(1) is the usual linear heat equation. The corresponding evolution is known in image

processing as a Gaussian Scale Space [1, 2, 3, 4]. In their seminal paper [5], Perona and Malik proposed nonlinear filters to bridge scale space and restoration ideas. Based on the observation that diffusion should not occur when the (local) gradient value is large (to avoid blurring the edges), they pointed out that nonlinear adaptive isotropic diffusion is achieved by replacing $C = 1$ by $C(u_f(\cdot, s))(\mathbf{x}) = c(\|\nabla_{\mathbf{x}} u_f(\mathbf{x}, s)\|)$, where $c : \mathbb{R}^+ \rightarrow \mathbb{R}^+$ is some smooth strictly decreasing positive function vanishing at infinity. An improvement of the Perona-Malik scheme is the “coherence-enhancing diffusion” (CED) introduced by Weickert [6] which additionally uses the direction of the gradient $\nabla_{\mathbf{x}} u_f$ leading to diffusion constant c being replaced by a nonlinear matrix.

However these methods often fail in image analysis applications with crossing or bifurcating curves as the direction of gradient at these structures is ill-defined, see [7] for more details. Scharr et al. in [8] present techniques which effectively deal with the particular case of X-junctions by relying on the 2-nd order jet of Gaussian derivatives in the image domain. Passing through higher order jets of Gaussian derivatives and induced Euclidean invariant differential operators does not allow one to generically deal with complex crossings and/or bifurcating structures. Instead we need gauge frames in higher dimensional affine Lie groups to deal with this issue. A gauge frame is a local coordinate system aligned/gauged with locally present (elongated) structures in an image. Differentiating w.r.t. such coordinates provides intrinsically natural derivatives as opposed to differentiating w.r.t. (artificially imposed) global coordinates. At interesting locations in the image, where multiple scale elongated structures cross, one needs multiple gauge frames. Therefore instead of gauge frames per position, $x \in \mathbb{R}^2$ in a (grey-scale) image $f : \mathbb{R}^2 \rightarrow \mathbb{R}$, we attach gauge frames to each Lie group element,

$$g = (x, t) \in G = \mathbb{R}^2 \rtimes T.$$

in a Coherent state (CS) transform $\mathcal{W}_\psi f : G \rightarrow \mathbb{C}$ of an image $f : \mathbb{R}^2 \rightarrow \mathbb{R}$. In this article we mainly consider $(G = SE(2), T = SO(2))$ and $(G = SIM(2), T = \mathbb{R}^+ \times SO(2))$, where (multiple scale) elongated structures are manifestly disentangled within the score, allowing for a crossing preserving flow (steered by gauge frames in the score). In medical image processing $\mathcal{W}_\psi f$ for $G = SE(2)$ is also referred to as an orientation score as it provides a score of how an image is decomposed out of local (possibly crossing) orientations.

1.1 Why extend to the $SIM(2)$ group?

In this paper we wish to extend the aforementioned orientation score framework to the case of the similitude group (group of planar translations, rotations and scaling), for the following reasons:

- Gauge frames based on Gaussian derivatives are usually aligned with a *single* Gaussian gradient direction, which is unstable in the vicinity of complex structures such as crossings and bifurcations. At these structures one needs multiple spatial frames per position. Therefore following the general idea of Scale spaces on affine Lie groups [9, 10, 11, 12], a natural next step would be to extend the domain of images to the affine Lie group $SIM(2) = \mathbb{R}^2 \rtimes (\mathbb{R}^+ \times SO(2))$ in order to have well posed gauge frames at crossing structures (adapted to multiple orientations and scales that are locally present).
- In the primary visual cortex both multiple scales and orientations are encoded per position. It is generally believed that receptive field profiles in neurophysiological experiments can be modelled by Gaussian derivatives [13, 14, 15, 16] and this provides a biological motivation to incorporate scales.
- Elongated (possibly crossing) structures often exhibit multiple scales. Earlier work by one of the authors [17, 7] proposes generic crossing preserving flows via invertible orientation scores (without explicit multiple scale decomposition). However, this approach treats all scales in the same way. As a result these flows do not always adequately deal with images containing elongated structures with strongly varying widths (scales). Therefore we must encode and process multiple scales in the scores.

Our framework involves the construction of a continuous wavelet transform of an image using the similitude group. This approach is related to that of directional wavelets [18, 19, 20, 21, 22] and curvelets [23, 24, 25, 26]. In particular the recent popular approach of shearlets [27, 28, 29, 30] also falls in the category of continuous

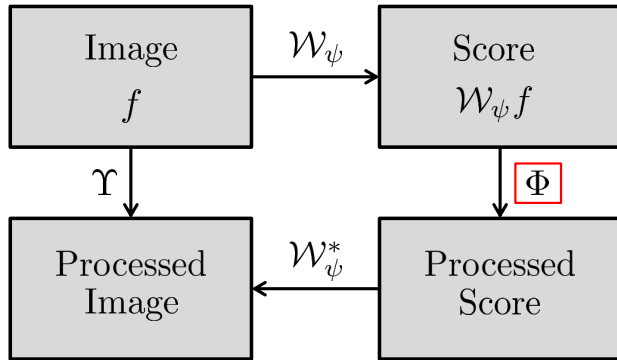


Figure 1: A schematic view on processing images $f : \mathbb{R}^2 \rightarrow \mathbb{R}$ via CS transform $\mathcal{W}_\psi f : G \rightarrow \mathbb{C}$ defined on Lie group $G = \mathbb{R}^2 \rtimes T$. Design of well posed transform \mathcal{W}_ψ and of appropriate operators Φ is the main objective of this article. Note that $\Upsilon = \mathcal{W}_\psi^* \circ \Phi \circ \mathcal{W}_\psi$, i.e. spatial processes are realized via invertible transforms akin to cortical columns in the visual brain [32].

wavelet transform but uses the shearlet group which includes the shearing, translation and scaling group. The main aim of this article is to construct rotation and translation invariant diffusion type flows on the wavelet transformed image. Although highly useful, the shearlet group (which is related to the similitude group by nilpotent approximations, see E) is not very suited for such exact rotation and translation covariant processing because of its group structure.

1.2 Our main results

There are two main motivating questions (see Figure 1) for the work presented in this article.

1. Can we design a well-posed invertible score, which is a complex-valued function on a Lie group $SIM(2)$, combining the strengths of directional wavelets [18, 19, 20], curvelets [23, 24, 25, 26] in such a way that allows for accurate and efficient implementation of subsequent contextual-enhancement operators?
2. Can we construct contextual flows in the wavelet domain, in order to ensure that only the wavelet coefficients that are coherent (from both probabilistic and group theoretical perspective, [31]) with the surrounding coefficients become dominant?

Our answer to both these questions is indeed affirmative. In the first part we follow the general approach by Grossmann, Morlet and Paul in [33], Ali in [31] and Führ in [34] we provide a short review of general results in the context of our case of interest. In practice there are upper/lower bounds on scaling and so in Theorem 4 and we provide stability analysis and condition number of a modified continuous wavelet transform on $SIM(2)$ which can be used for practical applications. The crucial point in our design is that we rely on explicit B-spline decomposition along log-polar type of coordinates in the Fourier domain. These are the canonical coordinates of the second type for $SIM(2)$, which are required for accurate left-invariant processing on the CS transformed images (scores). Figure 2 depicts the use of this wavelet transform in practice.

The latter and main part of this article is dedicated to answering the second question. Theorem 8 shows that only left-invariant operators on the transformed image correspond to Euclidean (and scaling) invariant operators on images. Therefore in this article we restrict ourselves to left-invariant PDE evolutions on $SIM(2)$. Theorem 11 provides a stochastic connection to our left-invariant flows in the wavelet domain. These flows are forward Kolmogorov equations corresponding to stochastic processes for multiple-scale contour enhancement on $SIM(2)$. Using the general theory of coercive operators on Lie groups, in Eq.(55) Gaussian estimates for the Green's function of linear diffusion on $SIM(2)$ are derived. In Eq.(58) we present nonlinear left-invariant adaptive diffusions on the image of a wavelet transform. Finally we present experiments to validate its practical advantages which become clear after comparisons with current state of the art enhancements.

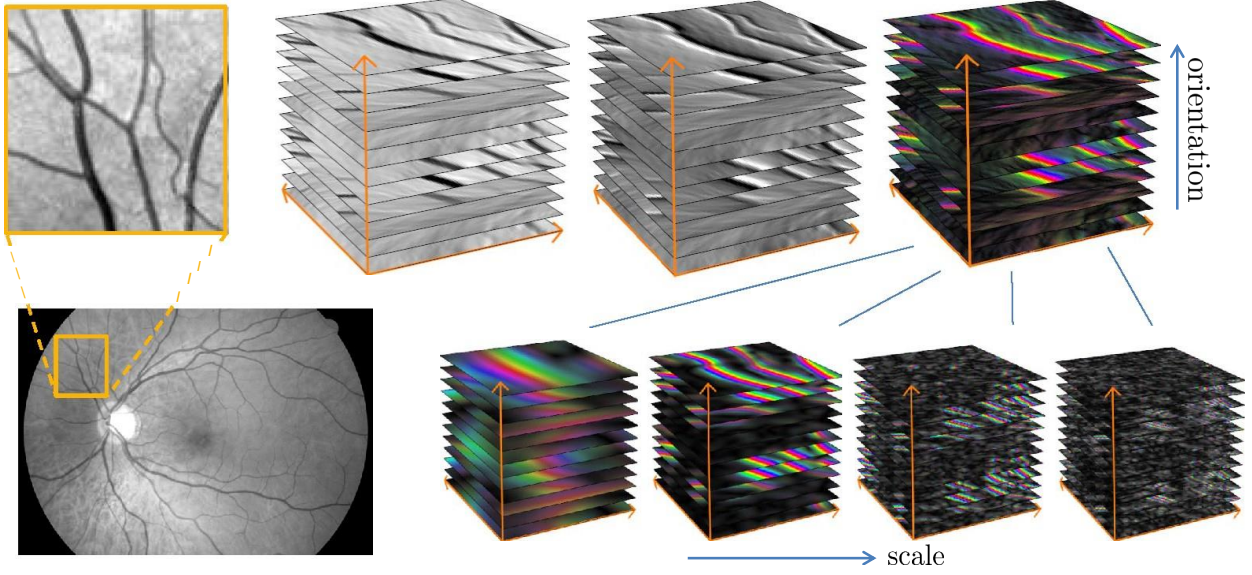


Figure 2: Top row: original image, the real-part of the CS transform on $SE(2)$ group reflects the centerlines, the imaginary part the edges of the bloodvessels, the combination (color represents phase direction and intensity represents the absolute value). Bottom row: visualizations of CW Transform on $SIM(2)$ group that allow us to include scale adaptation in our enhancement and detection.

1.3 Invertible Orientation Scores

Based on the early work by Ali, Antoine and Gazeau [22] and Kalitzin [35], Duits et al. [17, 12] introduced the framework of invertible orientation score in medical imaging to effectively handle the problem of generic crossing curves in the context of bio-medical applications. In this subsection we briefly explain the ideas developed in [17, 12].

The 2D-Euclidean motion group (i.e. the group of planar rotations and translations) $SE(2)$ is defined as $SE(2) = \mathbb{R}^2 \rtimes SO(2)$ where $SO(2)$ is the group of planar rotations. A CS transform, $U_f : SE(2) \rightarrow \mathbb{C}$ of an image $f : \mathbb{R}^2 \rightarrow \mathbb{R}$ is obtained by means of an anisotropic convolution kernel $\check{\psi} : \mathbb{R}^2 \rightarrow \mathbb{C}$ via

$$U_f(g) = \int_{\mathbb{R}^2} \overline{\check{\psi}(\mathbf{R}_\theta^{-1}(\mathbf{y} - \mathbf{x}))} f(\mathbf{y}) d\mathbf{y}, \quad g = (\mathbf{x}, \theta) \in SE(2),$$

where $\psi(-\mathbf{x}) = \check{\psi}(\mathbf{x})$ and $\mathbf{R}_\theta \in SO(2)$ is the 2D counter-clockwise rotation by angle $\theta \in [0, 2\pi)$. Assume $\psi \in \mathbb{L}_2(\mathbb{R}^2)$, then the transform \mathcal{W}_ψ which maps images $f \in \mathbb{L}_2(\mathbb{R}^2)$ can be rewritten as

$$U_f(g) = (\mathcal{W}_\psi f)(g) = (\mathcal{U}_g \psi, f)_{\mathbb{L}_2(\mathbb{R}^2)},$$

where $g \mapsto \mathcal{U}_g$ is a unitary (group-)representation of the Euclidean motion group $SE(2)$ into $\mathbb{L}_2(\mathbb{R}^2)$ given by $\mathcal{U}_g f(\mathbf{y}) = f(\mathbf{R}_\theta^{-1}(\mathbf{y} - \mathbf{x}))$ for all $g = (\mathbf{x}, \mathbf{R}_\theta) \in SE(2)$ and for all $f \in \mathbb{L}_2(\mathbb{R}^2)$. It is constructed by means of an admissible vector $\psi \in \mathbb{L}(\mathbb{R}^2)$ such that \mathcal{W}_ψ is unitary onto the unique reproducing kernel Hilbert space $\mathbb{C}_K^{SE(2)}$ of functions on $SE(2)$ with reproducing kernel $K(g, h) = (\mathcal{U}_g \psi, \mathcal{U}_h \psi)$, which is a closed vector subspace of $\mathbb{L}_2(SE(2))$. This leads to the essential Plancherel formula (see [31, 34])

$$\|\mathcal{W}_\psi f\|_{\mathbb{C}_K^{SE(2)}}^2 = \int_{\mathbb{R}^2} \int_0^{2\pi} |(\mathcal{F}\mathcal{W}_\psi f)(\omega, \theta)|^2 \frac{1}{M_\psi(\omega)} d\omega d\theta = \int_{\mathbb{R}^2} |(\mathcal{F}f)(\omega)|^2 d\omega = \|f\|_{\mathbb{L}_2(\mathbb{R}^2)}^2,$$

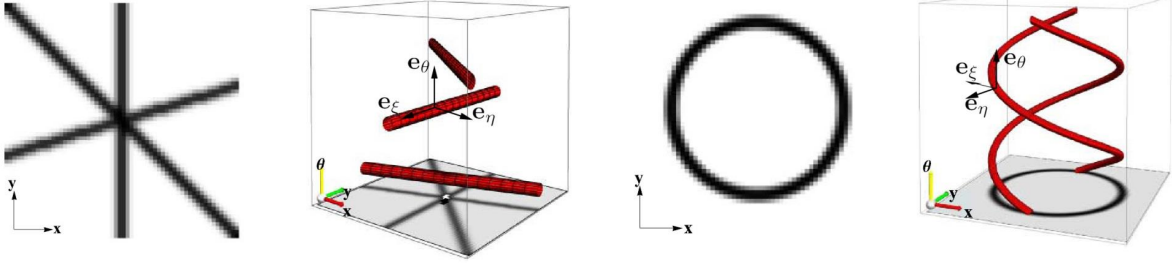


Figure 3: Illustration of a CS transform on $SE(2)$ for a crossing and a circle. This framework unwraps a crossing in the CS domain. In the case of the circle, the resulting response in a 3D visualization is a spiral since the orientation changes linearly as one traverses the circle. Note that the orientation dimension (displayed vertically) is 2π periodic.

where $M_\psi \in C(\mathbb{R}^2, \mathbb{R})$ is given by $M_\psi(\omega) = \int_0^{2\pi} |\mathcal{F}\psi(\mathbf{R}_\theta^T \omega)|^2 d\theta$. If ψ is chosen such that $M_\psi = 1$ then we gain \mathbb{L}_2 norm preservation. But this is not possible as $\psi \in \mathbb{L}_2(\mathbb{R}^2) \cap \mathbb{L}_1(\mathbb{R}^2)$ implies that M_ψ is a continuous function vanishing at infinity. In practice, however, because of finite grid sampling, \mathcal{U} is restricted to the space of disc limited images¹. Since the CS transform \mathcal{W}_ψ maps the space of images $\mathbb{L}_2(\mathbb{R}^2)$ unitarily onto the space $\mathbb{C}_K^{SE(2)}$ (provided $M_\psi > 0$) the original image $f : \mathbb{R}^2 \rightarrow \mathbb{R}$ can be reconstructed from U_f via the adjoint CS transform, $f = \mathcal{W}_\psi^* \mathcal{W}_\psi[f]$.

For examples of wavelets ψ for which $M_\psi = 1|_{B_{0,e}}$ and details on fast approximative reconstruction by integration over angles only, see [12]. For details on image processing (particularly enhancement and completion of crossing elongated structures) via CS transform on $SE(2)$ (orientation scores), see [37, 7, 38, 39]. An intuitive illustration of the relation between an elongated structure in a 2D image and the corresponding elongated structure in CS domain is given in Figure 3. In the top row of Figure 2 we also depict a practical example of this transform.

1.4 Structure of the article

This article is structured as follows.

- **(Section 2) Unitary CS transform on images:** Stability of the CS transform is discussed followed by an explicit construction of so called proper wavelets that allow for both a stable (re)construction of the transformed image and accurate implementation of subsequent left-invariant flows.
- **(Section 3) Operators on scores:** Employing the group structure in the wavelet domain a general framework for operators on the scores, involving left-invariant evolutions is discussed. These operators are interpreted in a differential geometric (and probabilistic) setting to provide a strong intuitive rationale for their choice.
- **(Section 4) Left-invariant diffusions:** Gaussian estimates for the Green's function of linear diffusion on $SIM(2)$ are derived followed by a discussion of non-linear adaptive diffusion.
- **(Section 5) Practical results:** In this section we present experiments that show the advantages of adaptive non-linear diffusion on multi-scale orientation scores in comparison to PDE techniques and previous work on orientation scores. Furthermore we compare our technique to state of the art denoising algorithms. Finally, we also apply these evolutions on well-established vesseness techniques and show benefits.

¹This requirement can be avoided in general by using distributional coherent transforms, for e.g. see [36, App.B].

2 Unitary operators between images and scores

In this section we present a quick overview of abstract coherent state transforms from a Hilbert space to a functional Hilbert space and thereby arrive at a continuous wavelet transform in our case of interest, the $SIM(2)$ group. This is followed by quantifying the stability of this transform in a sense which will be made precise. We end the section by explicitly constructing so called proper wavelets which would allow us to create appropriate PDE flows in the subsequent sections.

The continuous wavelet transform constructed by unitary irreducible representations of locally compact groups was first formulated by Grossman et al. [33]. Given a Hilbert space H and a unitary irreducible representation $g \mapsto \mathcal{U}_g$ of any locally compact group G in H , a nonzero vector $\psi \in H$ is called admissible if

$$C_\psi := \int_G \frac{|(\mathcal{U}_g \psi, \psi)|^2}{(\psi, \psi)_H} d\mu_G(g) < \infty, \quad (2)$$

where μ_G denotes the left invariant Haar measure on G . Given an admissible vector ψ and a unitary representation of a locally compact group G in a Hilbert space H , the CS transform $\widetilde{\mathcal{W}}_\psi : H \rightarrow \mathbb{L}_2(G)$ is defined by

$$(\widetilde{\mathcal{W}}_\psi[f])(g) = (\mathcal{U}_g \psi, f)_H.$$

It is well known in mathematical physics [31], that $\widetilde{\mathcal{W}}_\psi$ is a unitary transform onto a closed reproducing kernel space \mathbb{C}_K^G with $K_\psi(g, g') = \frac{1}{C_\psi} (\mathcal{U}_g \psi, \mathcal{U}_{g'} \psi)_H$ as an \mathbb{L}_2 -subspace. Note that we distinguish between the unitary wavelet transform $\widetilde{\mathcal{W}} : \mathbb{L}_2(\mathbb{R}^2) \rightarrow \mathbb{L}_2(G)$ and the isometric wavelet transform $\mathcal{W} : \mathbb{L}_2(\mathbb{R}^2) \rightarrow \mathbb{C}_K^G$ since the orthogonal projection onto \mathbb{C}_K^G is given by $\mathbb{P}_\psi = \widetilde{\mathcal{W}}_\psi \widetilde{\mathcal{W}}_\psi^*$ whereas $\mathcal{W}_\psi \mathcal{W}_\psi^* = I$.

2.1 Construction of a Unitary Map from H to \mathbb{C}_K^G

When G is a locally compact group the norm on \mathbb{C}_K^G has a simpler explicit form compared to usual description, see [12, Ch:7.2] and [40, Lemma 1.7]. One can give an explicit characterization of \mathbb{C}_K^G , in the case $G = \mathbb{R}^d \rtimes_\varphi T$, with T a linear algebraic group (for definition see [41]), \mathcal{U} the left-regular action of G onto $H = \mathbb{L}_2(\mathbb{R}^2)$ and thereby formulate a reconstruction theorem for affine groups. We call $\psi \in \mathbb{L}_2(\mathbb{R}^d)$ an admissible vector if

$$0 < M_\psi(\omega) := (2\pi) \int_T \left| \frac{\mathcal{F}[\mathcal{R}_t \psi(\omega)]}{\sqrt{\det(\varphi(t))}} \right|^2 d\mu_T(t) < \infty \text{ for almost every } \omega \in \Omega, \quad (3)$$

where \mathcal{R}_t for each $t \in T$ for any $f \in \mathbb{L}_2(\mathbb{R}^d)$ is defined as

$$\mathcal{R}_t f(x) = \frac{1}{\sqrt{\det(\varphi(t))}} f((\varphi(t)^{-1})x).$$

For an admissible vector $\psi \in H$, the span of $V_\psi = \{\mathcal{U}_g \psi | g \in G\}$, is dense in H . Further the corresponding CS transform $\mathcal{W}_\psi : H \rightarrow \mathbb{C}_K^G$ is unitary. This follows from general results in [34, Ch.5].

Theorem 1 *Let $G = \mathbb{R}^d \rtimes T$ and ψ be an admissible vector. Then $\mathcal{T}_{M_\psi} \Phi \in \mathbb{L}_2(G, d\mu_G(g))$ for all $\Phi \in \mathbb{C}_K^G$, where we define*

$$[\mathcal{T}_{M_\psi}[\Phi]](\mathbf{b}, t) := \mathcal{F}^{-1} \left[\omega \mapsto (2\pi)^{-d/4} M_\psi^{-1/2}(\omega) \mathcal{F}[\Phi(\cdot, t)](\omega) \right](\mathbf{b}).$$

Therefore $(\cdot, \cdot)_{M_\psi} : \mathbb{C}_K^G \times \mathbb{C}_K^G \rightarrow \mathbb{C}$ defined by

$$(\Phi, \Psi)_{M_\psi} = (\mathcal{T}_{M_\psi}[\Phi], \mathcal{T}_{M_\psi}[\Psi])_{\mathbb{L}_2(G)}, \quad (4)$$

is an explicit characterization of the inner product on \mathbb{C}_K^G , which is the unique functional Hilbert space with reproducing kernel $K : G \times G \rightarrow \mathbb{C}$ given by

$$K(g, h) = (\mathcal{U}_g \psi, \mathcal{U}_h \psi)_{\mathbb{L}_2(\mathbb{R}^d)} = (\mathcal{U}_{h^{-1}g} \psi, \psi)_{\mathbb{L}_2(\mathbb{R}^d)}, \quad g, h \in G. \quad (5)$$

The wavelet transformation $\mathcal{W}_\psi : H \rightarrow \mathbb{C}_K^G$ given by

$$\mathcal{W}_\psi[f](\mathbf{b}, t) = (\mathcal{U}_g \psi, f)_{\mathbb{L}_2(\mathbb{R}^d)}, \quad f \in \mathbb{L}_2(\mathbb{R}^d), \quad g = (\mathbf{b}, t) \in \mathbb{R}^d \rtimes_\varphi T, \quad (6)$$

is a unitary mapping from H to \mathbb{C}_K^G . The space \mathbb{C}_K^G is a closed subspace of the Hilbert space $\mathbb{H}_\psi \otimes \mathbb{L}_2(T; \frac{d\mu_T(t)}{\det(\varphi(t))})$, where

$$\mathbb{H}_\psi = \{f \in H \mid M_\psi^{-\frac{1}{2}} \mathcal{F}[f] \in \mathbb{L}_2(\mathbb{R}^d)\}$$

is equipped with the inner product

$$(f_1, f_2) = (M_\psi^{-\frac{1}{2}} \mathcal{F}[f_1], M_\psi^{-\frac{1}{2}} \mathcal{F}[f_2])_{\mathbb{L}_2(\mathbb{R}^d; (2\pi)^{-d/2} d\mathbf{x})}, \quad \text{for all } f_1, f_2 \in H.$$

The orthogonal projection \mathbb{P}_ψ of $\mathbb{H}_\psi \otimes \mathbb{L}_2(T; \frac{d\mu_T(t)}{\det(\varphi(t))})$ onto \mathbb{C}_K^G is given by $(\mathbb{P}_\psi[\Phi])(g) = (K(\cdot, g), \Phi)_{M_\psi}$.

Proof. See A for proof. \square

Remark 2 Since $\mathcal{W}_\psi : H \rightarrow \mathbb{C}_K^G$ is unitary, the inverse equals the adjoint and thus the image f can be reconstructed from its orientation score $\mathcal{W}_\psi[f]$ by

$$f = \mathcal{W}_\psi^*[\mathcal{W}_\psi[f]] = \mathcal{F}^{-1} \left[\omega \mapsto \frac{1}{(2\pi)^{d/2}} \int_T \mathcal{F}[\mathcal{W}_\psi[f](\cdot, t)](\omega) \mathcal{F}[\mathcal{R}_t \psi](\omega) \frac{d\mu_T}{|\det(\tau(t))|} M_\psi^{-1}(\omega) \right].$$

2.2 Coherent State Transform on the $SE(2)$ group (Orientation Score)

In this case $G = SE(2)$, $(\mathcal{U}_{g=(\mathbf{b}, \theta)} \psi)(\mathbf{x}) = \psi(\mathbf{R}_\theta^{-1}(\mathbf{x} - \mathbf{b}))$, $\Omega = \mathbb{R}^2$ and $H = \mathbb{L}_2(\mathbb{R}^2) \cap \mathbb{L}_1(\mathbb{R}^2)$ leading to [17, Thm 1]. For more details on construction as well operators in the coherent state domain see [38, 39]. For $\psi \in \mathbb{L}_2(\mathbb{R}^2) \cap \mathbb{L}_1(\mathbb{R}^2)$, M_ψ is a continuous function vanishing at infinity. Note that $C_\psi \neq M_\psi$ in this case as $M_\psi = 1$ and therefore unitary operator $\mathcal{W}_\psi : \mathbb{L}_2(\mathbb{R}^2) \rightarrow \mathbb{L}_2(SE(2))$ cannot be obtained. In order to deal with \mathbb{L}_1 -isometries one needs to either rely on distributions $\psi \in \mathbb{H}^{-s}(\mathbb{R}^2)$ with $s > 1$ and appropriate distributional wavelet transforms [36, App.B] or one needs to restrict to disc-limited images, which is appropriate for imaging applications.

2.3 Continuous Wavelet Transform on $SIM(2)$ group (Multiple Scale Orientation Scores)

Consider the case $T := SO(2) \times \mathbb{R}^+$, $G := SIM(2) = \mathbb{R}^2 \rtimes_\varphi (SO(2) \times \mathbb{R}^+)$ equipped with the group product

$$(\mathbf{x}, a, \theta)(\mathbf{x}', a', \theta') = (\mathbf{x} + \varphi(a, \theta)\mathbf{x}', aa', \theta + \theta'), \quad \text{for all } (\mathbf{x}, a, \theta), (\mathbf{x}', a', \theta') \in SIM(2), \quad (7)$$

where $\varphi(a, \theta) = a\mathbf{R}_\theta$. Consider the unitary representation of $SIM(2)$ in $\mathbb{L}_2(\mathbb{R}^2)$ given by,

$$\mathcal{U}_{g=(\mathbf{b}, a, \theta)} \psi(\mathbf{x}) = \frac{1}{a} \psi \left(\frac{\mathbf{R}_\theta^{-1}(\mathbf{x} - \mathbf{b})}{a} \right), \quad a > 0, \quad \theta \in [0, 2\pi], \quad \mathbf{b} \in \mathbb{R}^2, \quad (8)$$

We denote $\mathcal{U} : (\mathbf{x}, t) = (\mathbf{x}, a, \theta) \mapsto \mathcal{U}_{(\mathbf{x}, t)}$ as

$$\mathcal{U}_{\mathbf{x}, t} f = \mathcal{T}_{\mathbf{x}} \mathcal{R}_t f, \quad t = (a, \theta) \in \mathbb{R}^+ \times SO(2) \quad (9)$$

where $(\mathcal{T}_{\mathbf{x}}f)(\mathbf{x}') = f(\mathbf{x}' - \mathbf{x})$ and $(\mathcal{R}_t f)(\mathbf{x}') = \frac{1}{a} f(\frac{1}{a} \mathbf{R}_\theta \mathbf{x}')$ for all $\mathbf{x}, \mathbf{x}' \in \mathbb{R}^2$. In the continuous setting of $SIM(2)$ Theorem 1 yields

$$M_\psi(\boldsymbol{\omega}) = 2\pi \int_0^{2\pi} \int_{\mathbb{R}} |\hat{\psi}(e^\tau \mathbf{R}_\theta^{-1} \boldsymbol{\omega})|^2 d\tau d\theta = C_\psi, \quad (10)$$

and the reconstruction formula coincides with the known results on unitary CW transforms [33, 22]. Here we have used the notation $\hat{\psi} = \mathcal{F}\psi$.

2.4 Discrete Implementation

In this subsection we deal with the practical aspects of the implementation of the continuous wavelet transform discussed earlier. Recall that $SIM(2) = \mathbb{R}^2 \rtimes (SO(2) \times \mathbb{R}^+)$ where $T = (SO(2) \times \mathbb{R}^+)$ is a locally compact group. We can replace $SO(2)$ to be finite rotation group, denoted by \mathbb{T}_N (equipped with discrete topology) which is locally compact i.e.

$$\mathbb{T}_N = \{e^{iks_\varphi} | k \in \{0, 1, \dots, N-1\}, s_\varphi = \frac{2\pi}{N}\}, \text{ for } N \in \mathbb{N}, \quad (11)$$

and obtain $SE(2, N)$, see [42] for details. On the other hand the scaling group \mathbb{R}^+ cannot be written in terms of a finite scaling group as every finite subgroup of a multiplicative group of a field is a cyclic subgroup. Further from a practical point of view in the discrete case we need to have a lower and an upper bound on the choice of the scales. We assume that $a \in [a^-, a^+]$ where $0 < a^- < a^+$ and consider the following discretization for scales,

$$\mathbb{D}_M = \left\{ e^{(\tau^- + ls_\rho)} \middle| l \in \{0, 1, \dots, M-1\}, s_\rho = \frac{\tau^+ - \tau^-}{M} \right\}, \text{ for } M \in \mathbb{N}, \quad (12)$$

where $\tau^- = \log(a^-)$ and $\tau^+ = \log(a^+)$. Using the notation $\theta_k = ks_\varphi$ and $a_l = a^- e^{ls_\rho}$ we write the discrete version of (9)

$$U_f^{N,M}(\mathbf{b}, a_l, \theta_k) = (\mathcal{T}_{\mathbf{b}} \mathcal{R}_{(a_l, \theta_k)} \psi, f)_{\mathbb{L}_2(\mathbb{R}^2)}, \quad (13)$$

which is the discrete version of wavelet transform of an image $f \in \mathbb{L}_2(\mathbb{R}^2)$. The discrete version of M_ψ is,

$$M_\psi^D(\boldsymbol{\omega}) = \frac{1}{N} \frac{1}{M} \sum_{k=0}^{N-1} \sum_{l=0}^{M-1} \frac{1}{a} \hat{\psi}((a_l R_{\theta_k})^{-1} \boldsymbol{\omega}). \quad (14)$$

Note that in the discrete setting we are no longer in the unitary irreducible setting of [33] and M_ψ^D is not a constant (so $M_\psi^D \neq C_\psi$). Furthermore the space of wavelet transforms is embedded in $\mathbb{H}_\psi \otimes \mathbb{L}_2(SO(2) \times \mathbb{R}^+)$ instead of $\mathbb{L}_2(\mathbb{R}^2 \times SO(2) \times \mathbb{R}^+)$

2.5 Stable reconstruction of an image from OS

The unitarity result (Theorem 1) with $\mathbb{C}_K^{SIM(2)} \subset \mathbb{H}_\psi \otimes \mathbb{L}_2(SO(2) \times \mathbb{R}^+; \frac{d\mu_T(t)}{\det(\tau(t))})$ depends on the wavelet ψ . For stability estimates one requires \mathbb{L}_2 -norms on both the domain and the range. This means we must impose uniform lower and upper bounds in (3), which is possible only when we restrict the space of images to functions in $\mathbb{L}_2(\mathbb{R}^2) \cap \mathbb{L}_1(\mathbb{R}^2)$ whose Fourier transform is contained in an annulus. The space of these images is a Hilbert space given by,

$$\mathbb{L}_2^{\varrho^-, \varrho^+}(\mathbb{R}^2) = \{f \in \mathbb{L}_2(\mathbb{R}^2) | \text{supp}(\mathcal{F}[f]) \subset B_{0, \varrho^+} \setminus B_{0, \varrho^-}\}, \quad \varrho^+ > \varrho^- > 0, \quad (15)$$

where B_{0,ϱ^\pm} denotes a ball of radius ϱ^\pm around the origin in the Fourier domain. A practical motivation for the assumption of an upper bound (ϱ^+) on the support of the Fourier transform of the images is the Nyquist theorem, which states that *every band-limited function is determined by its values on a discrete grid*.

The value for ϱ^- directly relates to the coarsest scale we wish to detect in the spatial domain. Therefore the removal of extremely low frequencies from the image essentially corresponds to background removal in the image which is often an essential pre-processing step in medical image processing, see [43, 44].

We wish to construct a wavelet transform

$$\mathcal{W}_\psi^{\varrho^-, \varrho^+} : \mathbb{L}_2^{\varrho^-, \varrho^+}(\mathbb{R}^2) \rightarrow \mathbb{L}_2(\mathbb{R}^2 \times SO(2) \times \mathbb{R}^+) \quad (16)$$

which requires that (recall Eq.15),

$$\mathcal{U}_{\mathbf{x}, a, \theta} \psi \in \mathbb{L}_2^{\varrho^-, \varrho^+}(\mathbb{R}^2), \text{ where } a \in [a^-, a^+] \text{ and } \theta \in [0, 2\pi], \text{ with } a^+ > 1 > a^- \text{ such that } \frac{\varrho^-}{a^-} < \frac{\varrho^+}{a^+}.$$

We make the choice

$$\psi \in \mathbb{L}_1(\mathbb{R}^2) \cap \mathbb{L}_2(\mathbb{R}^2) \text{ with } \text{supp}(\mathcal{F}[\psi]) \subset B_{0, \varrho^+ / a^+} \setminus B_{0, \varrho^- / a^-} \quad (17)$$

and thus we have $\text{supp}(\mathcal{F}[\mathcal{U}_{\mathbf{x}, a, \theta} \psi]) \subset B_{0, \varrho^+} \setminus B_{0, \varrho^-}$, where $a \in [a^-, a^+]$ and $\theta \in [0, 2\pi]$.

Note that in our current context, $\psi \in \mathbb{L}_2^{\varrho^-, \varrho^+}(\mathbb{R}^2)$ is called an *admissible wavelet* if

$$0 < \widetilde{M}_\psi = (2\pi) \int_0^{2\pi} \int_{a^-}^{a^+} \left| \frac{\mathcal{F}[\mathcal{R}_{a, \theta} \psi]}{\sqrt{\det \tau(t)}} \right|^2 \frac{da}{a} d\theta < \infty \text{ on } B_{0, \varrho^+} \setminus B_{0, \varrho^-}, \quad (18)$$

where note that $M_\psi = C_\psi \neq \widetilde{M}_\psi$. By compactness of the set $[-\pi, \pi] \times [a^-, a^+]$ and assumption in Eq.(17) it follows that M_ψ is a continuous function vanishing at ∞ . We define, $SIM_+^- := \mathbb{R}^2 \times [-\pi, \pi] \times [a^-, a^+]$.

Definition 3 Let ψ be an admissible wavelet in the sense of (18). Then the wavelet transform $\mathcal{W}_\psi^{\varrho^-, \varrho^+} : \mathbb{L}_2^{\varrho^-, \varrho^+}(\mathbb{R}^2) \rightarrow \mathbb{L}^2(SIM_+^-)$ is given by

$$(\mathcal{W}_\psi^{\varrho^-, \varrho^+}[f])(g) = \frac{1}{a} \int_{\mathbb{R}^2} \overline{\psi \left(R_\theta^{-1} \left(\frac{\mathbf{y} - \mathbf{x}}{a} \right) \right)} f(\mathbf{y}) d\mathbf{y}, \quad f \in \mathbb{L}_2^{\varrho^-, \varrho^+}(\mathbb{R}^2),$$

for almost every $g = (\mathbf{x}, a, \theta) \in SIM_+^-$.

Quantification of Stability We quantify stability of an invertible linear transformation $A : V \rightarrow W$ from a Banach space $(V, \|\cdot\|_V)$ to a Banach space $(W, \|\cdot\|_W)$ via the condition number

$$\text{cond}(A) = \|A^{-1}\| \|A\| = \left(\sup_{\mathbf{x} \in V} \frac{\|\mathbf{x}\|_V}{\|A\mathbf{x}\|_W} \right) \left(\sup_{\mathbf{x} \in V} \frac{\|A\mathbf{x}\|_W}{\|\mathbf{x}\|_V} \right) \geq 1. \quad (19)$$

The closer it approximates 1, the more stable the operator and its inverse is. The condition number depends on the norms imposed on V and W . From a practical point of view, it is appropriate to impose the $\mathbb{L}_2(SIM_+^-)$ -norm instead of the reproducing kernel norm on the score since it does not depend on the choice of the wavelet ψ and we also use a \mathbb{L}_2 -norm on the space of images.

Theorem 4 Let ψ be an admissible wavelet, with $\widetilde{M}_\psi(\omega) > 0$ for all $\omega \in B_{0, \varrho^+} \setminus B_{0, \varrho^-}$. Then the condition number $\text{cond}(\mathcal{W}_\psi^{\varrho^-, \varrho^+})$ of $\mathcal{W}_\psi^{\varrho^-, \varrho^+} : \mathbb{L}_2^{\varrho^-, \varrho^+}(\mathbb{R}^2) \rightarrow \mathbb{L}_2(G)$, ($G = SIM_+^-$) defined by

$$\text{cond}(\mathcal{W}_\psi^{\varrho^-, \varrho^+}) = \|(\mathcal{W}_\psi^{\varrho^-, \varrho^+})^{-1}\| \|(\mathcal{W}_\psi^{\varrho^-, \varrho^+})\| = \left(\sup_{f \in \mathbb{L}_2^{\varrho^-, \varrho^+}(\mathbb{R}^2)} \frac{\|f\|_{\mathbb{L}_2(\mathbb{R}^2)}}{\|U_f\|_{\mathbb{L}_2(G)}} \right) \left(\sup_{f \in \mathbb{L}_2^{\varrho^-, \varrho^+}(\mathbb{R}^2)} \frac{\|U_f\|_{\mathbb{L}_2(G)}}{\|f\|_{\mathbb{L}_2(\mathbb{R}^2)}} \right)$$

satisfies

$$1 \leq (\text{cond}(\mathcal{W}_\psi^{\varrho^-, \varrho^+}))^2 \leq \left(\sup_{\varrho^- \leq \|\omega\| \leq \varrho^+} \widetilde{M}_\psi^{-1}(\omega) \right) \left(\sup_{\varrho^- \leq \|\omega\| \leq \varrho^+} \widetilde{M}_\psi(\omega) \right).$$

Proof. Since $\widetilde{M}_\psi > 0$ and is continuous on the compact set $B_{0, \varrho^+} \setminus B_{0, \varrho^-} = \{\omega \in \mathbb{R}^2 \mid \varrho^- \leq \|\omega\| \leq \varrho^+\}$, $\sup_{\varrho^- < \|\omega\| < \varrho^+} \widetilde{M}_\psi(\omega) = \max_{\varrho^- < \|\omega\| < \varrho^+} \widetilde{M}_\psi(\omega)$ do exist. The same holds for \widetilde{M}_ψ^{-1} . Furthermore for all $f \in \mathbb{L}_2^{\varrho^-, \varrho^+}(\mathbb{R}^2)$, the restriction of the corresponding wavelet transform to fixed orientations and scales also belong to the same space, i.e. $U_f(\cdot, a, e^{i\theta}) \in \mathbb{L}_2^{\varrho^-, \varrho^+}(\mathbb{R}^2)$, where $\theta \in [0, 2\pi]$, $a \in [a^-, a^+]$. Using $\check{\psi}(x) = \psi(-x)$,

$$(\mathcal{W}_\psi f)(\mathbf{x}, t) = \int_{\mathbb{R}^2} \overline{\mathcal{R}_t \check{\psi}(\mathbf{x} - \mathbf{x}')} f(\mathbf{x}') d\mathbf{x}' = (\overline{\mathcal{R}_t \check{\psi}} *_{\mathbb{R}^2} f)(\mathbf{x}) = (\mathcal{F}^{-1}(\overline{\mathcal{F} \mathcal{R}_t \check{\psi} \mathcal{F}} f))(\mathbf{x}), \quad (20)$$

which gives, $\mathcal{F}[U_f](\omega) = \mathcal{F}[\overline{\mathcal{R}_t \check{\psi}}](\omega) \mathcal{F}[f](\omega)$. By Theorem 1 we have $\|f\|_{\mathbb{L}_2(\mathbb{R}^2)}^2 = \|U_f\|_{M_\psi}^2 := (U_f, U_f)_{M_\psi}$,

$$\begin{aligned} (\text{cond}(\mathcal{W}_\psi^{\varrho^-, \varrho^+}))^2 &= \left(\sup_{f \in \mathbb{L}_2^{\varrho^-, \varrho^+}(\mathbb{R}^2)} \frac{\|U_f\|_{\widetilde{M}_\psi}}{\|U_f\|_{\mathbb{L}_2(G)}} \right) \left(\sup_{f \in \mathbb{L}_2^{\varrho^-, \varrho^+}(\mathbb{R}^2)} \frac{\|U_f\|_{\mathbb{L}_2(G)}}{\|U_f\|_{\widetilde{M}_\psi}} \right) \\ &\leq \left(\sup_{\varrho^- \leq \|\omega\| \leq \varrho^+} \widetilde{M}_\psi^{-1}(\omega) \right) \left(\sup_{\varrho^- \leq \|\omega\| \leq \varrho^+} \widetilde{M}_\psi(\omega) \right). \end{aligned}$$

Finally we note that $1 = \|(\mathcal{W}_\psi^{\varrho^-, \varrho^+})^{-1}(\mathcal{W}_\psi^{\varrho^-, \varrho^+})\| \leq \|(\mathcal{W}_\psi^{\varrho^-, \varrho^+})^{-1}\| \|(\mathcal{W}_\psi^{\varrho^-, \varrho^+})\|$. \square

Corollary 5 *The stability of the (inverse) wavelet transformation $\mathcal{W}_\psi^{\varrho^-, \varrho^+} : \mathbb{L}_2^{\varrho^-, \varrho^+}(\mathbb{R}^2) \rightarrow \mathbb{L}_2(\text{SIM}_+)$ is optimal if $\widetilde{M}_\psi(\omega) = \text{constant}$ for all $\omega \in \mathbb{R}$, with $\varrho^- \leq \|\omega\| \leq \varrho^+$.*

In case $\widetilde{M}_\psi \approx 1_{B_{0, \varrho^+} \setminus B_{0, \varrho^-}}$, the reconstruction formula can be simplified to,

$$f \approx \mathcal{F}^{-1} \left[\omega \mapsto \frac{1}{(2\pi)} \int_{a^-}^{a^+} \int_0^{2\pi} \mathcal{F}[U_f(\cdot, a, e^{i\theta})](\omega) \mathcal{F}[\mathcal{R}_{a, e^{i\theta}} \psi](\omega) d\theta \frac{da}{a} \right]. \quad (21)$$

2.6 Design of Proper Wavelets

In this sequel a wavelet $\psi \in \mathbb{L}_2(\mathbb{R}^2) \cap \mathbb{L}_1(\mathbb{R}^2)$ with \widetilde{M}_ψ smoothly approximating $1_{B_{0, \varrho^+} \setminus B_{0, \varrho^-}}$, is called a **proper wavelet**. The entire class of proper wavelets allows for a lot of freedom in the choice of ψ . In practice it is mostly sufficient to consider wavelets that are similar to the long elongated patch one would like to detect and orthogonal to structures of local patches which should not be detected, in other words employing the basic principle of template matching. We restrict the possible choices by listing below certain practical requirements to be fulfilled by our transform.

1. The wavelet transform should yield a finite number of orientations (N) and scales (M).
2. The wavelet should be strongly directional, in order to obtain sharp responses on oriented structures.
3. The transformation should handle lines, contours and oriented patterns. Thus the wavelet should pick up edge, ridge and periodic profiles.
4. In order to pick up local structures, the wavelet should be localized in spatial domain.

To ensure that the wavelet is strongly directional and minimizes uncertainty in $\text{SIM}(2)$, we require that the support of the wavelet be contained in a convex cone in the Fourier domain, [18]. The following lemma gives a simple but practical approach to obtain proper wavelets ψ , with $M_\psi = 1_{B_{0, \varrho^+} \setminus B_{0, \varrho^-}}$.

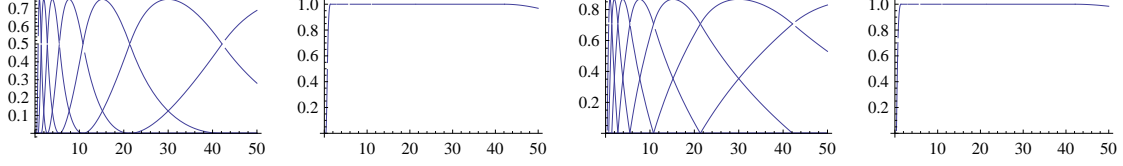


Figure 4: Plot for the B-splines described in (27). Values chosen: $a^- = \varrho^- = 10^{-8}$, $a^+ = \varrho^+ = 50$, $N_s = 7$. See Eq. (27), (28) for details. From Left to Right: (4.1) Plot of 3rd order B-splines i.e. $k = 3$. The B-splines are skewed because of non linear sampling in the scale dimension; (4.2) Summing over the B-splines; (4.3) Plot of square root of the B-splines; (4.4) Summing over the square root of B-Splines.

Lemma 6 Let τ^-, τ^+ be chosen such that $\tau^- = \log(a^-)$ and $\tau^+ = \log(a^+)$, where $0 < a \in [a^-, a^+]$ is the finite interval of scaling. Let $A : SO(2) \rightarrow \mathbb{R}^+$ and $B : [\tau^-, \tau^+] \rightarrow \mathbb{R}^+$ such that

$$2\pi \int_0^{2\pi} A(\varphi) d\varphi = 1, \quad \int_{\tau^-}^{\tau^+} B(\rho) d\rho = 1, \quad (22)$$

then the wavelet $\psi = \mathcal{F}^{-1}[\omega \rightarrow \sqrt{A(\varphi)B(\rho)}]$ has $\widetilde{M}_\psi(\omega) = 1$ for all $\omega = (\rho \cos \varphi, \rho \sin \varphi) \in B_{0,\varrho^+} \setminus B_{0,\varrho^-}$.

Proof. From (10) and (18), for all $\omega \in B_{0,\varrho^+} \setminus B_{0,\varrho^-}$ we have,

$$M_\psi(\omega) = 2\pi \int_0^{2\pi} \int_{\varrho^-}^{\varrho^+} |\hat{\psi}(e^\tau \mathbf{R}_\theta^{-1} \omega)|^2 d\tau d\theta = 2\pi \int_0^{2\pi} \int_{\varrho^-}^{\varrho^+} |\sqrt{A(\varphi - \theta)B(e^\tau \rho)}|^2 d\tau d\theta = 1. \quad \square$$

Lemma 6 can be translated into the discrete framework, recall (11) and (12), making condition (22),

$$\frac{1}{N} \sum_{k=0}^{N-1} A(\varphi - \theta_k) = 1 \text{ and } \frac{1}{M} \sum_{l=0}^{M-1} B(e^{\tau_l} \rho) = 1. \quad (23)$$

where we have made use of discrete notations introduced in (13). If $2\pi \int_0^{2\pi} \sqrt{A(\varphi)} d\varphi \approx 1$ and $\int_{\tau^-}^{\tau^+} \sqrt{B(\rho)} d\rho \approx 1$, we have a fast and simple approximative reconstruction:

$$\begin{aligned} \tilde{f}(\mathbf{x}) &= 2\pi \int_0^{2\pi} \int_{\tau^-}^{\tau^+} (\mathcal{W}_\psi f)(\mathbf{x}, \tau, \theta) d\tau d\theta \approx \mathcal{F}^{-1}[\omega \mapsto (\sqrt{\widetilde{M}_\psi} * \mathcal{F}[f](\omega))](\mathbf{x}), \text{ for a.e. } \omega \in B_{0,\varrho^+} \setminus B_{0,\varrho^-}. \\ \sqrt{\widetilde{M}_\psi} &\approx 1_{B_{0,\varrho^+} \setminus B_{0,\varrho^-}} \Rightarrow \tilde{f} \approx f \in \mathbb{L}_2^{\varrho^-, \varrho^+}(\mathbb{R}^2). \end{aligned} \quad (24)$$

We need to fulfil the requirement $\widetilde{M}_\psi(\omega) \approx 1$ with an appropriate choice of kernel satisfying the additional condition $\sqrt{\widetilde{M}_\psi} \approx 1$. The idea is to “fill the cake by pieces of cake” in the Fourier domain. In order to avoid high frequencies in the spatial domain, these pieces must be smooth and they must overlap. A choice of B-spline based functions in the angular and the log-radial direction is an appropriate choice for such a wavelet kernel. This design of wavelets in the Fourier domain is similar to the framework of curvelets [24, 25, 26]. However, our decomposition of unity in the Fourier domain is more suited for the subsequent design of left-invariant diffusions in the wavelet domain. The reason for us to choose log-polar B-spline decomposition is that the canonical coordinates of the second kind in $SIM(2)$ are given by

$$\xi = a(x \cos \theta + y \sin \theta), \quad \eta = a(-x \sin \theta + y \cos \theta), \quad \theta, \tau = \log_e a,$$

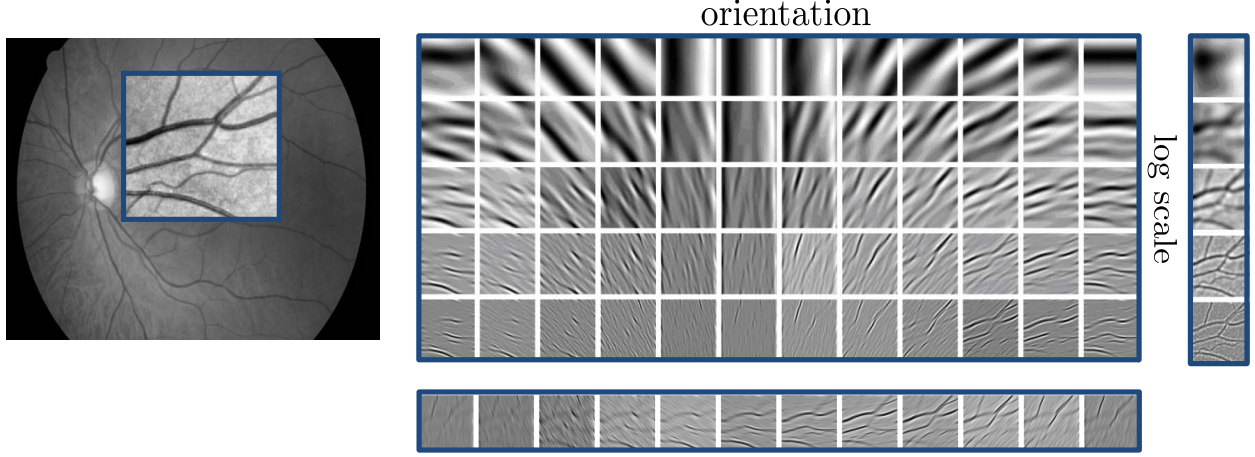


Figure 5: Scale-OS of a retinal image. As shown, Scale-OS can be used to create the Orientation Score and Gaussian-Scale Space of the image.

and it will turn out that our subsequent evolutions are best expressed in these coordinates. We would also like to point out that a similar construction which involves mixing different levels of scale selectivity was presented in [45].

The k^{th} order B-spline denoted by B^k is defined as

$$B^k(x) = (B^{k-1} * B^0)(x), \quad B^0(x) = \begin{cases} 1 & \text{if } -1/2 < x < +1/2 \\ 0 & \text{otherwise} \end{cases} \quad (25)$$

with the property that B-splines add up to 1. For more details see [46]. Based on the requirements and considerations above we propose the following kernel

$$\psi(\mathbf{x}) = \mathcal{F}_{\mathbb{R}^2}^{-1}[\omega \rightarrow \sqrt{A(\varphi)B(\rho)}](\mathbf{x})G_{\sigma_s}(\mathbf{x}), \quad (26)$$

where G_{σ_s} is a Gaussian window that enforces spatial locality cf. requirement 5. $A : \mathbb{T} \rightarrow \mathbb{R}^+$ and $B : [\varrho^-, \varrho^+] \rightarrow \mathbb{R}^+$ are defined as,

$$A(\varphi) = B^k\left(\frac{(\varphi \bmod 2\pi) - \pi/2}{s_\varphi}\right), \quad B(\varrho) = B^k\left(\frac{\log[\rho]}{s_\rho}\right), \quad (27)$$

where $s_\varphi = \frac{2\pi}{N}$ and $s_\rho = (\log[a^+] - \log[a^-])/M$ where M is the number of chosen scales and a^- , a^+ are predefined scales, based on ϱ^- , ϱ^+ respectively. See Figure 4 for a plot of these log B-splines and note that

$$\sum_{l=0}^{M-1} B^k\left(\frac{\log[\rho]}{s_\rho} + l + \frac{\tau^-}{s_\rho}\right) = 1 \text{ and } \sum_{l=0}^{M-1} \sqrt{B^k\left(\frac{\log[\rho]}{s_\rho} + l + \frac{\tau^-}{s_\rho}\right)} \approx 1. \quad (28)$$

3 Operators on Scores

There exists a 1-to-1 correspondence between bounded operators $\Phi \in \mathcal{B}(\mathbb{C}_K^C)$ on the range of CW transform and bounded operators $\Upsilon \in \mathcal{B}(\mathbb{L}_2(\mathbb{R}^d))$ given by

$$\Upsilon[f] = (\mathcal{W}_\psi^* \circ \Phi \circ \mathcal{W}_\psi)[f], \quad f \in \mathbb{L}_2(\mathbb{R}^d), \quad (29)$$

which allows us to relate operations on transformed images to operations on images in a robust manner. To get a schematic view of the operations see Figure 1. By Theorem 1 that the range of the unitary wavelet transform $\mathcal{W}_\psi : \mathbb{L}_2(\mathbb{R}^2) \rightarrow \mathbb{C}_K^G$ is a subspace of $\mathbb{L}_2(G)$. For proper wavelets we have (approximative) \mathbb{L}_2 -norm preservation and therefore $\mathbb{L}_2(G) \cong \mathbb{H}_\psi$ (with $\mathbb{L}_2(G) = \mathbb{H}_\psi$ if $M_\psi = 1$). In general if, $\Phi : \mathbb{L}_2(G) \rightarrow \mathbb{C}_K^G$ is a bounded operator then the range need not be contained in \mathbb{C}_K^G . Therefore we also consider $\widetilde{\mathcal{W}}_\psi : \mathbb{L}_2(\mathbb{R}^d) \rightarrow \mathbb{L}_2(G)$ given by $\widetilde{\mathcal{W}}_\psi f = \mathcal{W}_\psi f$. Its adjoint is given by,

$$(\widetilde{\mathcal{W}}_\psi)^*(V) = \int_G \mathcal{U}_g \psi V(g) d\mu_G(g), \quad V \in \mathbb{L}_2(G).$$

The operator $\mathbb{P}_\psi = \widetilde{\mathcal{W}}_\psi (\widetilde{\mathcal{W}}_\psi)^*$ is the orthogonal projection on the space \mathbb{C}_K^G whereas $\mathcal{W}_\psi \mathcal{W}_\psi^* = I$. This projection can be used to decompose operator Φ :

$$\Phi(U_f) = \mathbb{P}_\psi(\Phi(U_f)) + (I - \mathbb{P}_\psi)(\Phi(U_f)).$$

Notice that the orthogonal complement $(\mathbb{C}_K^G)^\perp$, which equals $\mathcal{R}(I - \mathbb{P}_\psi)$, is exactly the null-space of $(\widetilde{\mathcal{W}}_\psi)^*$ as $\mathcal{N}((\widetilde{\mathcal{W}}_\psi)^*) = \mathcal{N}((\mathcal{W}_\psi)^*) = (\mathcal{R}(\mathcal{W}_\psi))^\perp = (\mathbb{C}_K^G)^\perp$ and so

$$[(\widetilde{\mathcal{W}}_\psi)^* \circ \Phi \circ \widetilde{\mathcal{W}}_\psi][f] = [(\widetilde{\mathcal{W}}_\psi)^* \circ \mathbb{P}_\psi \circ \Phi \circ \widetilde{\mathcal{W}}_\psi][f], \quad (30)$$

for all $f \in \mathbb{L}_2(\mathbb{R}^2)$ and all $\Phi \in \mathcal{B}(\mathbb{L}_2(G))$, so we see that the net operator associated to $\Phi : \mathbb{L}_2(G) \rightarrow \mathbb{L}_2(G)$ is given by $\mathbb{P}_\psi \circ \Phi : \mathbb{L}_2(G) \rightarrow \mathbb{C}_K^G$. In the reminder of this section we present design principles for Υ .

3.1 Design Principles

We now formulate a few desirable properties of Υ , and sufficient conditions for Φ that guarantee that Υ meets these requirements.

1. **Covariance with respect to rotation, translation and scaling:**

$$\Upsilon \circ \mathcal{U}_g^{SIM(2)} = \mathcal{U}_g^{SIM(2)} \circ \Upsilon, \quad \forall g = (x, y, \tau, \theta) \in SIM(2). \quad (31)$$

This is an important requirement because the net operations on images should not be affected by rotation and translation of the original image. Typically, this is achieved by restricting one self to left-invariant operators Φ . Often we will omit scaling covariance in Eq.(31) as in many imaging applications this is not natural and therefore we require (31) only to hold for the $SE(2)$ subgroup.

2. **Left invariant vector fields:** In order to achieve the Euclidean invariance mentioned above, we need to employ left invariant vector fields on $SIM(2)$ as a moving frame of reference.

3. **Nonlinearity:** The requirement that Υ commute with \mathcal{U} immediately rules out linear operators Φ . Recall that \mathcal{U} is irreducible, and by Schur's lemma [47], any linear intertwining operator is a scalar multiple of the identity operator.

4. **Left-invariant parabolic evolutions on the Similitude group:** We consider the following two types of evolutions which include the wavelet transform as a initial condition.

- Combine linear diffusions with monotone operations on the co-domain
- Non linear adaptive diffusion

5. **Probabilistic models for contextual multi-scale feature propagation in the wavelet domain:** Instead of uncorrelated soft-thresholding of wavelet coefficients we aim for PDE flows that amplify the wavelet coefficients which are probabilistically coherent w.r.t. neighbouring coefficients. This coherence w.r.t. neighbouring coefficients is based on underlying stochastic processes (random walks) for multiple-scale contour enhancement.

In Subsections 3.2-3.5 we will elaborate on these design principles.

3.2 Covariance with respect to Rotations and Translations

Let $G = \mathbb{R}^d \rtimes T$ denote an arbitrary affine Lie-group.

Definition 7 An operator $\Phi : \mathbb{L}_2(G) \rightarrow \mathbb{L}_2(G)$ is left invariant iff

$$\Phi[\mathcal{L}_h f] = \mathcal{L}_h[\Phi f], \text{ for all } h \in G, f \in \mathbb{L}_2(\mathbb{R}^2), \quad (32)$$

where the left regular action \mathcal{L}_g of $g \in G$ onto $\mathbb{L}_2(G)$ is given by

$$\mathcal{L}_g \psi(h) = \psi(g^{-1}h). \quad (33)$$

Theorem 8 Let $\Phi : \mathbb{C}_K^G \rightarrow \mathbb{L}_2(G)$ be a bounded operator. Then the unique corresponding operator Υ on H given by $\Upsilon[f] = (\widetilde{\mathcal{W}_\psi})^* \circ \Phi \circ \widetilde{\mathcal{W}_\psi}[f]$ is Euclidean (and scaling) invariant, i.e. $\mathcal{U}_g \Upsilon = \Upsilon \mathcal{U}_g$ for all $g \in G$ if and only if $\mathbb{P}_\psi \circ \Phi$ is left invariant, i.e. $\mathcal{L}_g(\mathbb{P}_\psi \circ \Phi) = (\mathbb{P}_\psi \circ \Phi) \mathcal{L}_g$, for all $g \in G$.

Proof. See Appendix B for proof. \square

Practical Consequence: Now let us return to our case of interest $G = SIM(2)$, where $H = \mathbb{L}_2(\mathbb{R}^2)$. Euclidean invariance of Υ is of great practical importance, since the result of operators on scores should not be essentially different if the original image is rotated or translated. In addition in our construction scaling the image also does not affect the outcome of the operation. The latter constraint may not always be desirable in applications.

Remark 9 Other CW transform based approaches such as shearlets also carry a group structure. However this is a different group structure corresponding for e.g. with the shearing, translation and scaling group. Although such a group structure follows by a contraction (see E (75)) it is not suited for exact rotation and translation covariant processing.

3.3 Left Invariant Vector fields (differential operators) on $SIM(2)$

Left invariant differential operators are crucial in the construction of appropriate left-invariant evolutions on $G = SIM(2)$. Similar to Definition 7, the right regular action \mathcal{R}_g of $g \in G$ onto $\mathbb{L}_2(G)$ is defined by

$$\mathcal{R}_g \psi(h) = \psi(hg), \quad \forall g, h \in G, \psi \in \mathbb{L}_2(G). \quad (34)$$

A vector field (now considered as a differential operator²) \mathcal{A} on a group G is called left-invariant if it satisfies

$$\mathcal{A}_g \phi = \mathcal{A}_e(\phi \circ L_g) = \mathcal{A}_e(h \mapsto \phi(gh)),$$

for all smooth functions $\phi \in C_c^\infty(\Omega_g)$ where Ω_g is an open set around $g \in G$ and with the left multiplication $L_g : G \rightarrow G$ given by $L_g h = gh$. The linear space of left-invariant vector fields $\mathcal{L}(G)$ equipped with the Lie product $[\mathcal{A}, \mathcal{B}] = \mathcal{A}\mathcal{B} - \mathcal{B}\mathcal{A}$ is isomorphic to $T_e(G)$ by means of the isomorphism,

$$T_e(G) \ni A \leftrightarrow \mathcal{A} \in \mathcal{L}(G) \Leftrightarrow \mathcal{A}_g(\phi) = A(\phi \circ L_g) = A(h \mapsto \phi(gh)) = (L_g)_* A(\phi)$$

for all smooth $\phi : G \supset \Omega_g \rightarrow \mathbb{R}$.

We define an operator $d\mathcal{R} : T_e(G) \rightarrow \mathcal{L}(G)$,

$$(d\mathcal{R}(A)\phi)(g) := \lim_{t \downarrow 0} \frac{(\mathcal{R}_{\exp(tA)}\phi)(g) - \phi(g)}{t}, \quad A \in T_e(G), \phi \in \mathbb{L}_2(G), g \in G, \quad (35)$$

²Any tangent vector $X \in T(G)$ can be considered as a differential operator acting on a function $U : G \rightarrow \mathbb{R}$. So, for instance, if we are using $X_e \in T_e(G)$ in the context of differential operators, all occurrences of \mathbf{e}_i will be replaced by ∂_i , which is the short-hand notation for $\frac{\partial}{\partial x_i}$. See [48] for the equivalence between these two viewpoints.

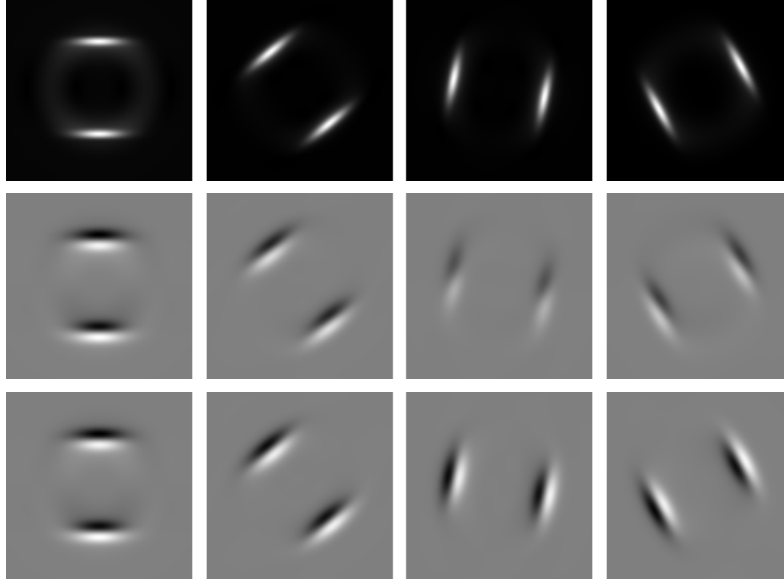


Figure 6: The difference between cartesian derivatives and left-invariant derivatives, shown on a scale-OS (at a fixed scale) of an image with a single circle. From left to right, several orientations are shown. Row 1: Scale-OS of a circle image at a fixed scale; Row 2: Cartesian derivative ∂_y ; Row 3 : Left-invariant derivative ∂_η . Comparing the derivatives ∂_y and ∂_η (Column 3) we observe that ∂_η is invariant under rotation, i.e. the interpretation of ∂_η stays the same.

and where \mathcal{R} and \exp are the right regular representation and the exponential map respectively. Using $d\mathcal{R}$ we obtain the corresponding basis for left-invariant vector fields on G :

$$\{\mathcal{A}_1, \mathcal{A}_2, \mathcal{A}_3, \mathcal{A}_4\} := \{d\mathcal{R}(A_1), d\mathcal{R}(A_2), d\mathcal{R}(A_3), d\mathcal{R}(A_4)\}, \quad (36)$$

or explicitly in coordinates

$$\{\mathcal{A}_1, \mathcal{A}_2, \mathcal{A}_3, \mathcal{A}_4\} = \{\partial_\theta, \partial_\xi, \partial_\eta, \partial_\beta\} = \{\partial_\theta, a(\cos \theta \partial_x + \sin \theta \partial_y), a(-\sin \theta \partial_x + \cos \theta \partial_y), a \partial_a\}, \quad (37)$$

where we use the short notation $\partial_a := \frac{\partial}{\partial a}$ for the partial derivatives and where,

$$\{\mathcal{A}_1|_e, \mathcal{A}_2|_e, \mathcal{A}_3|_e, \mathcal{A}_4|_e\} = \{A_1, A_2, A_3, A_4\} = \{\partial_\theta, \partial_x, \partial_y, \partial_a\}.$$

To simplify the scale related left invariant differential operator, we introduce a new variable, $\tau = \log a$, which leads to the following change in left invariant derivatives

$$\{\mathcal{A}_1, \mathcal{A}_2, \mathcal{A}_3, \mathcal{A}_4\} = \{\partial_\theta, e^\tau (\cos \theta \partial_x + \sin \theta \partial_y), e^\tau (-\sin \theta \partial_x + \cos \theta \partial_y), \partial_\tau\}. \quad (38)$$

The set of differential operators $\{\mathcal{A}_1, \mathcal{A}_2, \mathcal{A}_3, \mathcal{A}_4\} = \{\partial_\theta, \partial_\xi, \partial_\eta, \partial_\tau\}$ is the appropriate set of differential operators to be used in orientation scores because all $SIM(2)$ -coordinate independent linear and nonlinear combinations of these operators are left invariant. Furthermore at each scale ∂_ξ is always the spatial derivative tangent to the orientation θ and ∂_η is always orthogonal to this orientation. Figure 6 illustrates this for ∂_η versus ∂_y . It is important to note that unlike derivatives $\{\partial_x, \partial_y, \partial_a, \partial_\theta\}$ which commute, the left-invariant derivatives $\{\partial_\xi, \partial_\eta, \partial_\tau, \partial_\theta\}$ do not commute. However these operators satisfy the same commutator relations as their Lie algebra counterparts as $d\mathcal{R}$ generates a Lie-algebra isomorphism

$$[A_i, A_j] = \sum_{k=1}^4 c_{ij}^k A_k \leftrightarrow [\mathcal{A}_i, \mathcal{A}_j] = \mathcal{A}_i \mathcal{A}_j - \mathcal{A}_j \mathcal{A}_i = \sum_{k=1}^4 c_{ij}^k \mathcal{A}_k, \quad (39)$$

where c_{ij}^k are the structure constants.

An exponential curve is obtained by using the **exp** mapping of the Lie algebra elements, i.e. an exponential curve passing through the identity element $e \in SIM(2)$ at $t = 0$ can be written as

$$\gamma_c(t) = \exp \left(t \sum_{i=1}^4 c^i \mathcal{A}_i \Big|_{g=e} \right) = \exp \left(t \sum_{i=1}^4 c^i A_i \right), \quad (40)$$

and an exponential curve passing through $g_0 \in SIM(2)$ can be obtained by left multiplication with $g_0 = (x_0, y_0, e^{\tau_0}, \theta_0)$, i.e. $g_0 \gamma_c(t)$. The following theorem applies the method of characteristics (for PDEs) to transport along exponential curves. The explicit formulation is important because left-invariant convection-diffusion on $SIM(2)$ takes place only along exponential curves, see Theorem 22.

Theorem 10 *Let $A \in T_e(SIM(2))$. Then the following holds.*

1. $U \in \mathcal{D}(d\mathcal{R}(A)) \Rightarrow \mathcal{R}_{e^{tA}} U \in \mathcal{D}(d\mathcal{R}(A))$, where $\mathcal{D}(X)$ denotes the domain of operator X .
2. $e^{td\mathcal{R}(A)} = \mathcal{R}_{e^{tA}}$, $\forall t > 0$ where $d\mathcal{R}$ is defined in (35).
3. $\gamma_c(t) = g_0 \exp \left(t \sum_{i=1}^4 c^i A_i \right)$ are the characteristics for the following PDE,

$$\frac{\partial W(g, t)}{\partial t} = - \sum_{i=1}^4 c^i \mathcal{A}_i W(g, t), \quad W(g, 0) = U. \quad (41)$$

Proof. See D for proof. □

The exponential map defined on $T_e(SIM(2))$ is bijective, and so we can define the logarithm mapping, $\log = (\exp)^{-1} : SIM(2) \rightarrow T_e(SIM(2))$. For proof see [20, Chap. 4]. For the explicit formulation of the exponential and logarithm curves in our case see C. The explicit form of the log map will be used to approximate the solution for linear evolutions on $SIM(2)$ in Section 4.1.

3.4 Quadratic forms on Left Invariant vector fields

We apply the general theory of evolutions (convection-diffusion) on Lie groups, [9], to the $SIM(2)$ group and consider the following left-invariant second-order evolution equations,

$$\begin{cases} \partial_t W(g, t) = Q^{\mathbf{D}, \mathbf{a}}(\mathcal{A}_1, \mathcal{A}_2, \mathcal{A}_3, \mathcal{A}_4) W(g, t), \\ W(\cdot, t = 0) = \mathcal{W}_\psi f(\cdot), \end{cases} \quad (42)$$

where $W : SIM(2) \times \mathbb{R}^+ \rightarrow \mathbb{C}$ and $Q^{\mathbf{D}, \mathbf{a}}$ is given by

$$Q^{\mathbf{D}, \mathbf{a}}(\mathcal{A}_1, \mathcal{A}_2, \mathcal{A}_3, \mathcal{A}_4) = \sum_{i=1}^4 \left(-a_i \mathcal{A}_i + \sum_{j=1}^4 D_{ij} \mathcal{A}_i \mathcal{A}_j \right), \quad a_i, D_{ij} \in \mathbb{R}, \quad \mathbf{D} := [D_{ij}] \geq 0, \quad \mathbf{D}^T = \mathbf{D}. \quad (43)$$

Throughout this article we restrict ourselves to the diagonal case with $a_1 = a_2 = a_4 = 0$. This is a natural choice when a_i and D_{ij} are constant, as we do not want to impose a-priori curvature and a-priori scaling drifts in our flows. However, when adapting D and a to the initial condition (i.e. wavelet transform data) such restrictions are not necessary. In fact, practical advantages can be obtained when choosing D diagonal w.r.t. optimal gauge frame, [7, 39]. Choosing $D_{ij} = D_{ii} \delta_{ij}$, $i, j \in \{1, 2, 3, 4\}$, the quadratic form becomes,

$$Q^{\mathbf{D}, \mathbf{a}}(\mathcal{A}_1, \mathcal{A}_2, \mathcal{A}_3, \mathcal{A}_4) = [-a_1 \partial_\theta - a_2 \partial_\xi - a_3 \partial_\eta - a_4 \partial_\tau + D_{11}(\partial_\theta)^2 + D_{22}(\partial_\xi)^2 + D_{33}(\partial_\eta)^2 + D_{44}(\partial_\tau)^2]. \quad (44)$$

The first order part of (44) takes care of transport (convection) along the exponential curves, deduced in Section 3.3. The second order part takes care of diffusion in the $SIM(2)$ group. Note that these evolution equations are left-invariant by construction.

Hörmander in [49] gave necessary and sufficient conditions on the convection and diffusion parameters, respectively $a = (a_1, a_2, a_3, a_4)$ and $\mathbf{D} = D_{ij}$, in order to get smooth Green's functions of the left-invariant convection-diffusion equation (42) with generator (44). By these conditions the non-commutative nature of $SIM(2)$ in certain cases takes care of missing directions in the diffusion tensor. Applying the Hörmander's theorem [49] produces necessary and sufficient conditions for smooth (resolvent) Green's functions on $SIM(2) \setminus \{e\}$ on the diffusion and convection parameters (\mathbf{D}, a) in the generator (44) of (42) for diagonal \mathbf{D} :

$$\{1, 2, 4\} \subset \{i \mid a_i \neq 0 \vee D_{ii} \neq 0\} \vee \{1, 3, 4\} \subset \{i \mid a_i \neq 0 \vee D_{ii} \neq 0\}. \quad (45)$$

A covariant derivative of a co-vector field \mathbf{a} on the manifold $(SIM(2), \mathcal{G})$ is a $(0, 2)$ -tensor field with components $\nabla_j a_i = \mathcal{A}_j a_i - \Gamma_{ij}^k a_k$, whereas the covariant derivative of a vector field \mathbf{v} on $SIM(2)$ is a $(1, 1)$ -tensor field with components $\nabla_{j'} v^i = \mathcal{A}_{j'} v^i + \Gamma_{j'k'}^i v^{k'}$, where we have made use of the notation $\nabla_j := D_{\mathcal{A}_j}$, when imposing the Cartan connection (tangential to the $SE(2)$ -case in [39], $SE(3)$ -case in [50] and the $H(2d+1)$ -case in [11]). The Christoffel symbols equal minus the (anti-symmetric) structure constants of the Lie algebra $\mathcal{L}(SIM(2))$, i.e. $\Gamma_{ij}^k = -c_{ij}^k$. The left-invariant equations (42) with a diagonal diffusion tensor (44) can be rewritten in covariant derivatives as

$$\begin{cases} \partial_s W(g, s) = \sum_{i,j=1}^4 \mathcal{A}_i((D_{ij}(W))(g, s)) \mathcal{A}_j W(g, s) = \sum_{i,j=1}^4 \nabla_i((D_{ij}(W))(g, s)) \nabla_j W(g, s), \\ W(g, 0) = \mathcal{W}_\psi f(g), \text{ for all } g \in SIM(2), s > 0. \end{cases} \quad (46)$$

Both convection and diffusion in the left-invariant evolution equations (42) take place along the exponential curves in $SIM(2)$ which are covariantly constant curves with respect to the Cartan connection. For proof and various details see F.

3.5 Probabilistic models for contextual feature propagation

Section 3.4 described the general form of convection-diffusion operators on the $SIM(2)$ group. For the particular case of contour enhancement i.e. diffusion on the $SIM(2)$ group, which corresponds to the choice $D_{ij} = D_{ii} \delta_{ij}$, $i, j \in \{1, 2, 3, 4\}$, $D_{33} = 0$ and $\mathbf{a} = \mathbf{0}$, we have the following result.

Theorem 11 *The evolution on $SIM(2)$ given by*

$$\begin{cases} \partial_t W(g, t) = [D_{11}(\partial_\theta)^2 + D_{22}(\partial_\xi)^2 + D_{44}(\partial_\tau)^2] W(g, t), \\ W(\cdot, t = 0) = \mathcal{W}_\psi f(\cdot), \end{cases} \quad (47)$$

is the forward Kolmogorov (Fokker-Planck) equation of the following stochastic process for multi-scale contour enhancement

$$\begin{cases} \mathbf{X}(s) = \mathbf{X}(0) + \sqrt{2D_{22}\epsilon_2} \int_0^s (\cos(\Theta(t))e_x + \sin(\Theta(t))e_y) e^{\mathfrak{T}(t)} d(\sqrt{t}) \\ \Theta(s) = \Theta(0) + \sqrt{s}\sqrt{2D_{11}}\epsilon_1 \\ \mathfrak{T}(s) = \mathfrak{T}(0) + \sqrt{s}\sqrt{2D_{44}}\epsilon_4, \end{cases} \quad (48)$$

where $e_1, e_2, e_4 \sim \mathcal{N}(0, 1)$ are the standard random variables and $D_{11}, D_{22}, D_{44} > 0$.

In order to avoid technicalities regarding probability measures on Lie groups, see [51] for details, we only provide a short and basic explanation which covers the essential idea of the proof.

The stochastic differential equation in (48) can be considered as limiting case of the following discrete stochastic processes on $SIM(2)$:

$$\begin{cases} G_{n+1} := (\mathbf{X}_{n+1}, \Theta_{n+1}, \mathfrak{T}_{n+1}) = G_n + \sqrt{\Delta s} \sum_{i=1,2,4} \sum_{j=1,2,4} \frac{\epsilon_{i,n+1}}{\sqrt{N}} \sqrt{2D_{ii}} e_i|_{G_n}, \\ G_0 = (\mathbf{X}_0, \Theta_0, \mathfrak{T}_0), \end{cases} \quad (49)$$

where $n = 1, \dots, N-1$, $N \in \mathbb{N}$ denotes the number of steps with step-size $\Delta s > 0$, $\{\epsilon_{i,n+1}\}_{i=1,2,4}$ are independent normally distributed $\epsilon_{i,n+1} \sim \mathcal{N}(0, 1)$ and $e_j|_{G_n} \equiv \mathcal{A}_j|_{G_n}$, i.e.

$$e_1|_{G_n} = \begin{pmatrix} 0 \\ 0 \\ 0 \\ 1 \end{pmatrix}, \quad e_2|_{G_n} = \begin{pmatrix} e^{\mathfrak{T}} \cos \Theta \\ e^{\mathfrak{T}} \sin \Theta \\ 0 \\ 0 \end{pmatrix}, \quad e_3|_{G_n} = \begin{pmatrix} -e^{\mathfrak{T}} \sin \Theta \\ e^{\mathfrak{T}} \cos \Theta \\ 0 \\ 0 \end{pmatrix}, \quad e_4|_{G_n} = \begin{pmatrix} 0 \\ 0 \\ 1 \\ 0 \end{pmatrix}.$$

Note that the continuous process (48) directly arises from the discrete process (49) by recursion and taking the limit $N \rightarrow \infty$.

4 Left-invariant Diffusions on $SIM(2)$

Following our framework of stochastic left-invariant evolutions on $SIM(2)$ we will restrict ourselves to contour enhancement, where the Forward-Kolmogorov equation is essentially a hypo-elliptic diffusion on the $SIM(2)$ group and therefore we recall (47)

$$\begin{cases} \partial_t W(g, t) = [D_{11}(\partial_\theta)^2 + D_{22}(\partial_\xi)^2 + D_{44}(\partial_\tau)^2] W(g, t), \\ W(\cdot, t=0) = \mathcal{W}_\psi f(\cdot). \end{cases} \quad (50)$$

In the remainder of this paper we study linear diffusion (combined with monotone operations on the co-domain) and non-linear diffusion on the $SIM(2)$ group in the context of our imaging application.

4.1 Approximate Contour Enhancement Kernels for Linear Diffusion on Scale-OS

In [37, 38], the authors derive the exact Green's function of (42) for the $SE(2)$ case. To our knowledge explicit and exact formulae for heat kernels of linear diffusion on $SIM(2)$ do not exist in the literature. However using the general theory in [52, 53], one can compute Gaussian estimates for Green's function of left-invariant diffusions on Lie groups. As a first step this involves approximating $SIM(2)$ by a parametrized class of groups $(SIM(2))_q$, $q \in [0, 1]$ in between $SIM(2)$ and the nilpotent Heisenberg approximation $SIM(2)_0$. This idea of contraction has been explained in E.

According to the general theory in [53], the heat-kernels $K_t^{q, \mathbf{D}} : (SIM(2))_q \rightarrow \mathbb{R}^+$ (i.e. kernels for contour enhancement whose convolution yields diffusion on $(SIM(2))_q$) on the parametrized class of groups $(SIM(2))_q$, $q \in [0, 1]$ in between $SIM(2)$ and $(SIM(2))_0$ satisfy the Gaussian estimates

$$|K_t^{q, \mathbf{D}}(g)| \leq Ct^{-\frac{5}{2}} \exp\left(\frac{-b\|g\|_q^2}{4t}\right), \quad \text{with } C, b > 0 \text{ (constant)}, g \in (SIM(2))_q, \quad (51)$$

where the norm $\|\cdot\|_q : (SIM(2))_q \rightarrow \mathbb{R}^+$ is given by $\|g\|_q = |\log_{(SIM(2))_q}(g)|_q$. $\log_{(SIM(2))_q} : (SIM(2))_q \rightarrow T_e((SIM(2))_q)$, is the logarithmic mapping on $(SIM(2))_q$, which is computed explicitly for the case of $(SIM(2))_{q=1} = SIM(2)$ in C, and where the weighted modulus, see [53, Prop 6.1], in our special case of interest is given by,

$$\left| \sum_{i=1}^4 c_q^i A_i^q \right| = \sqrt{|c_q^1|^{2/w_1} + |c_q^2|^{2/w_2} + |c_q^3|^{2/w_3} + |c_q^4|^{2/w_4}} = \sqrt{((c_q^1)^2 + (c_q^2)^2 + (c_q^4)^2) + |c_q^3|}, \quad (52)$$

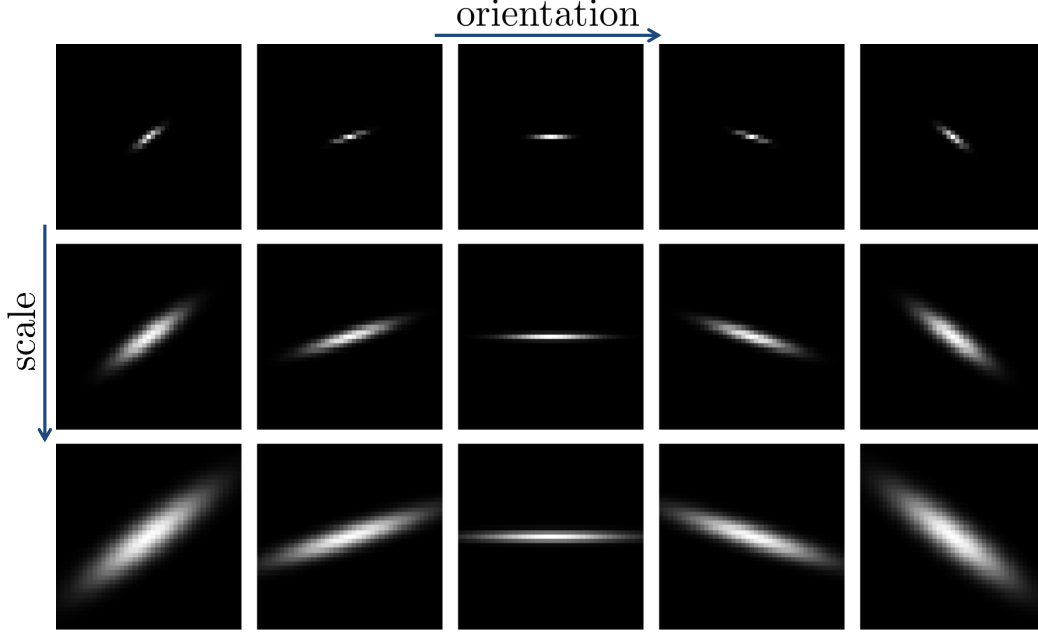


Figure 7: Plots of enhancement kernels generated on a 41×41 grid at different scales and orientations. Parameters chosen: $D_{11} = 0.05$, $D_{22} = 1$, $D_{44} = 0.01$, $t = 0.7$.

where recall the weightings from (70).

Remark 12 The constants b , C in (51) can be taken into account by the transformations $t \mapsto \frac{t}{b}$, $f \mapsto Cf$.

A sharp estimate for the front factor constant C in (51) is given by

$$C = \frac{1}{4\pi D_{11} D_{22}} \frac{1}{\sqrt{D_{44}}}. \quad (53)$$

This follows from the general theory in [53] where the choice of constant C is uniform for all groups $(SIM(2))_q$, $q \in [0, 1]$. Thus to determine C we need to determine the front factor constant for the green's function G of the following resolvent equation

$$((D_{11}(\mathcal{A}_1^0)^2 + D_{22}(\mathcal{A}_2^0)^2 + D_{44}(\mathcal{A}_4^0)^2)) G(x, y, \tau, \theta) = +\delta_e$$

where \mathcal{A}^0 denote the basis for $\mathcal{L}(H)$ (recall $H = (SIM(2))_{q \downarrow 0}$) and e is the identity of H . Using $[D_{11}(\mathcal{A}_1^0)^2 + D_{22}(\mathcal{A}_2^0)^2, (\mathcal{A}_4^0)^2] = 0$ and the results in [38] arrive at

$$|K_t^{q=1, \mathbf{D}}(g)| \leq \frac{1}{4\pi t^{\frac{5}{2}} D_{11} D_{22} \sqrt{D_{44}}} \exp \left(\frac{-1}{4t} \left(\frac{\theta^2}{D_{11}} + \frac{(c^2(g))^2}{D_{22}} + \frac{\tau^2}{D_{44}} + \frac{|c^3(g)|}{\sqrt{D_{11} D_{22} D_{44}}} \right) \right), \quad (54)$$

where recall the explicit formulae for c^i , $i \in \{2, 3\}$ from C,

$$c^2(g) = \frac{(y\theta - x\tau) + (-\theta\eta + \tau\xi)}{t(1 + e^{2\tau} - 2e^\tau \cos\theta)}, \quad c^3(g) = \frac{-(x\theta + y\tau) + (\theta\xi + \tau\eta)}{t(1 + e^{2\tau} - 2e^\tau \cos\theta)}.$$

A problem with these estimates is that they are not differentiable everywhere. This problem can be solved by using the estimate

$$|a| + |b| \geq \sqrt{a^2 + b^2} \geq \frac{1}{\sqrt{2}}(|a| + |b|),$$

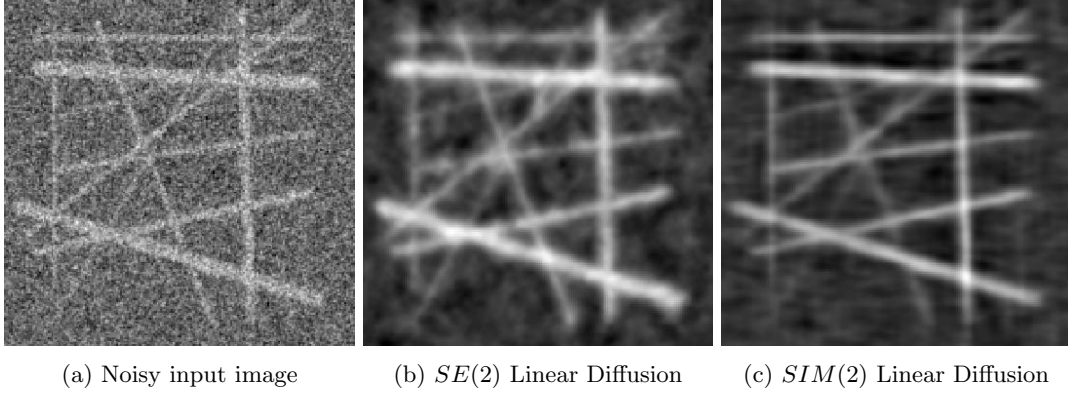


Figure 8: Comparison of enhancement via linear diffusion using Gaussian estimates for heat kernels on $SE(2)$ and $SIM(2)$. Left: Original image, Center: Enhancement via Linear diffusion on $SE(2)$ group using Gaussian estimates in [38], Right: Enhancement via Linear diffusion on $SIM(2)$ group using estimate in (55). Parameters- OS: $N_\theta = 20, N_s = 5$; $SE(2)$ estimate: $D_{11} = 0.05, D_{22} = 1, t = 3$; $SIM(2)$ estimate: $D_{11} = 0.05, D_{22} = 1, D_{44} = 0.01, t = 0.7$.

which holds for all $a, b \in \mathbb{R}$, to the exponents of our Gaussian estimates. Thus we estimate the weighted modulus by the equivalent (for all $q > 0$) weighted modulus $|\cdot|_q : T_e((SIM(2))_q) \rightarrow \mathbb{R}^+$ by $\left| \sum_{i=1}^4 c_q^i A_i^q \right|_q := \sqrt[4]{((c_q^1)^2 + (c_q^2)^2 + (c_q^4)^2)^2 + |c_q^3|^2}$, yielding the Gaussian estimate,

$$|K_t^{q=1, D}(g)| \leq \frac{1}{4\pi t^{\frac{5}{2}} D_{11} D_{22} \sqrt{D_{44}}} \exp \left(\frac{-1}{4t} \left(\left[\frac{\theta^2}{D_{11}} + \frac{(c^2(g))^2}{D_{22}} + \frac{\tau^2}{D_{44}} \right]^2 + \frac{|c^3(g)|^2}{D_{11} D_{22} D_{44}} \right) \right). \quad (55)$$

Figure 7 shows the typical structure of these enhancement kernels.

Remark 13 When cascading group convolutions and transformations in the co-domain of the scores one can generalize the scattering operators by Mallat et al. on \mathbb{R}^n , see [54, 55], to left-invariant scattering operators on affine Lie groups such as $SIM(2)$ which would provide us with stability under local deformations.

In practice, medical images exhibit complicated structures which require local adaptivity per group location via gauge frames. This brings us to non-linear diffusions that we will solve numerically in the next section.

4.2 Nonlinear Left Invariant Diffusions on $SIM(2)$

Adaptive nonlinear diffusion on the 2D Euclidean motion group $SE(2)$ called coherence enhancing diffusion on orientation scores (CED-OS) was introduced in [7, 38]. We wish apply this adaptive $SE(2)$ diffusion to each scale in our scale-OS, which is possible because at a fixed scale the scale-OS is a function on the $SE(2)$ group. Next we present a brief outline of the CED-OS algorithm and then apply it to our case of interest.

4.2.1 CED-OS - Brief Outline

CED-OS involves the following two steps:

- *Curvature Estimation.* Curvature estimation of a spatial curve is based on the optimal exponential curve fit at each point. We find the best exponential curve fit (and the corresponding curvature) to the data $(x, y, \theta) \mapsto |(\mathcal{W}_\psi f)(x, y, \theta)|$ by using the exponential map,

$$t \mapsto \exp(t(c_*^1 A_1 + c_*^2 A_2 + c_*^3 A_3)) \text{ with } (c_*^1)^2 + \beta^2 (c_*^2)^2 + \beta^2 (c_*^3)^2 = 1,$$

via the techniques explained in [39, 7] and summarized in G.

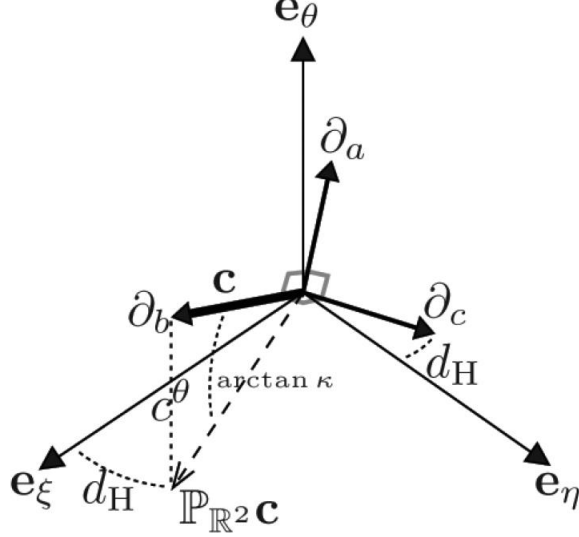


Figure 9: Illustration of curvature κ and deviation from horizontality d_H and the gauge frame (56). Note that $e_\theta \leftrightarrow \partial_\theta$, $e_\xi \leftrightarrow \partial_\xi$, $e_\eta \leftrightarrow \partial_\eta$.

- *Adaptive curvatures based diffusion scheme using gauge coordinates.* The best exponential curve fit mentioned above is parametrized by $\mathbf{c}_* = (c_*^1, c_*^2, c_*^3) \in \mathbb{R}^3$ which provides us the curvature κ (and deviation from horizontality d_H if we do not impose $c_*^3 = 0$). In fact it furnishes a whole set of gauge frames $\{\partial_a, \partial_b, \partial_c\}$ as can be seen in Figure 9. The gauge frames in spherical coordinates read

$$\begin{aligned}\partial_a &= -\cos \alpha \cos d_H \partial_\xi - \cos \alpha \sin d_H \partial_\eta + \beta \sin \alpha \partial_\theta, \\ \partial_b &= \sin \alpha \cos d_H \partial_\xi + \sin \alpha \sin d_H \partial_\eta + \beta \cos \alpha \partial_\theta, \\ \partial_c &= -\sin d_H \partial_\xi + \cos d_H \partial_\eta.\end{aligned}\tag{56}$$

The resulting nonlinear evolution equations on orientation scores is

$$\begin{cases} \partial_t U(g, t) = \begin{pmatrix} \beta \partial_\theta & \partial_\xi & \partial_\eta \end{pmatrix} M_{\alpha, d_H}^T \begin{pmatrix} D_{aa} & 0 & 0 \\ 0 & D_{bb} & 0 \\ 0 & 0 & D_{cc} \end{pmatrix} M_{\alpha, d_H} \begin{pmatrix} \beta \partial_\theta \\ \partial_\xi \\ \partial_\eta \end{pmatrix} U(g, t), \quad t > 0, \\ U(g, t = 0) = \mathcal{W}_\psi[f](g) \text{ for all } g \in SE(2), \end{cases}\tag{57}$$

where we use the shorthand notation $D_{ii} = (D_{ii}(U))(g, t)$, for $i = a, b, c$. The matrix

$$M_{\alpha, d_H} = \begin{pmatrix} \sin \alpha & -\cos \alpha \cos d_H & -\cos \alpha \sin d_H \\ \cos \alpha & \cos d_H \sin \alpha & \sin \alpha \sin d_H \\ 0 & -\sin d_H & \cos d_H \end{pmatrix}$$

is the rotation matrix in $SO(3)$ that maps the left-invariant vector fields $\{\beta \partial_\theta, \partial_\xi, \partial_\eta\}$ onto the gauge frame $\{\partial_a, \partial_b, \partial_c\}$.

Figure 10 depicts the dependence of the corresponding local linear diffusion kernel on curvature and orientation strengths. Eq.(57) is implemented by a Euler forward scheme (expressed by finite differences along the moving frame of reference while relying on B-spline approximations yielding better rotation covariance [56][Pg.142]) involving the parameters $(\tilde{\rho}, \rho_s, c, \beta)$,

$$U_{n+1} = \Delta t (QU_n) + U_n,$$

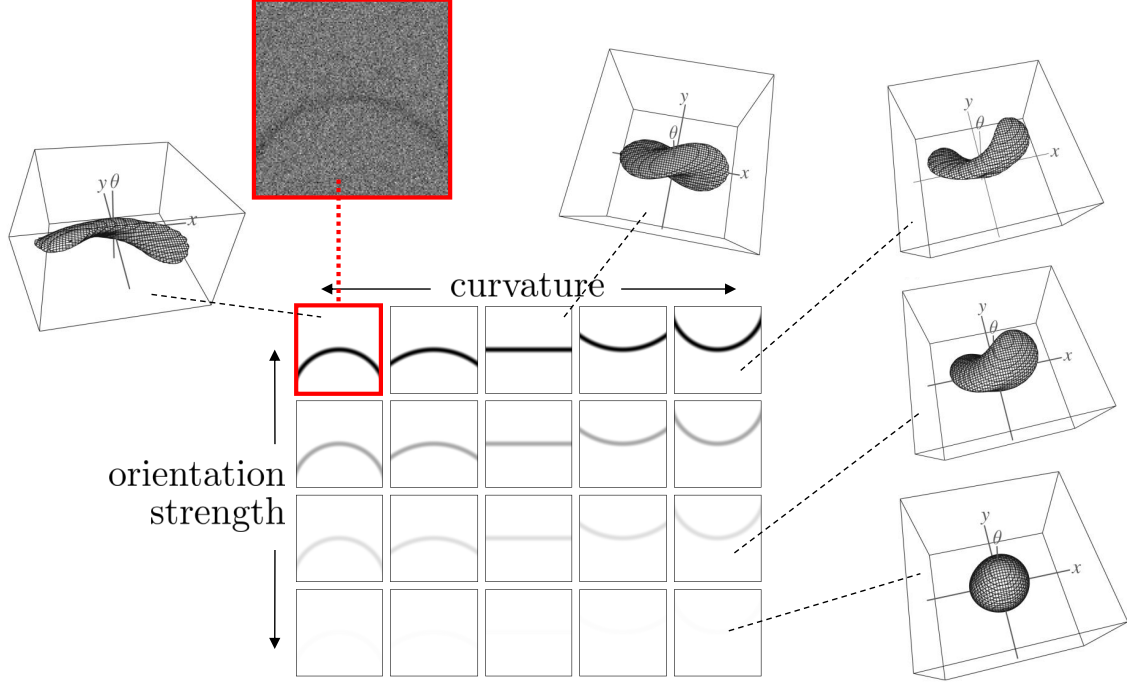


Figure 10: Illustration of heat kernels $K_t^D : SE(2) \rightarrow \mathbb{R}^+$ on $SE(2)$ corresponding to varying curvature and orientation strengths. As orientation strength decreases the kernels become more isotropic (needed for noise reduction) and as curvature increases the diffusion kernels in $SE(2)$ bend accordingly.

where $U_n = U(\cdot, \cdot, t_n)$ with discrete time steps and the generator is given by,

$$(QU)(\cdot, \cdot, t) = \left(\beta \partial_\theta^D \partial_\xi^D \partial_\eta^D \right) M_{\alpha, d_H}^T \left(G_{\rho_s, \rho_s, \rho_s \beta^2} * \begin{pmatrix} D_{aa}(U(\cdot, \cdot, t)) & 0 & 0 \\ 0 & D_{bb}(U(\cdot, \cdot, t)) & 0 \\ 0 & 0 & D_{cc}(U(\cdot, \cdot, t)) \end{pmatrix} \right) M_{\alpha, d_H} \begin{pmatrix} \beta \partial_\theta^D \\ \partial_\xi^D \\ \partial_\eta^D \end{pmatrix},$$

where $G_{\rho_s, \rho_s, \rho_s \beta^2}(x, y, \theta)$ denotes a Gaussian kernel, which is isotropic on each spatial plane with spatial scale $\rho_s = \frac{1}{2} \sigma_s^2$ and anisotropic with scale $\rho_s \beta^2$ in orientation. Here ∂_j^D denotes the left-invariant finite difference operator in the j^{th} direction implemented via B-spline interpolation [7]. Furthermore we set $D_{bb} = 0$, $(D_{aa}U)(\cdot, \cdot, t) = (D_{cc}U)(\cdot, \cdot, t) = e^{-\frac{(s(U)(\cdot, \cdot, t))^2}{c}}$, $c > 0$, with the orientation confidence $s(U(\cdot, \cdot, t)) = (\partial_a^2 + \partial_b^2)U(\cdot, \cdot, t)$. The derivatives ∂_a, ∂_b are Gaussian derivatives, computed with scales $(\tilde{\rho}, \tilde{\rho}, \tilde{\rho} \beta^2)$, orthogonal to locally optimal direction with c being the eigenvector of the Hessian matrix corresponding to best exponential curve fit, where we enforce horizontality [7] by setting $d_H = 0$ (see Figure 10).

4.2.2 CED-OS on Scale-OS (CED-SOS)

For an image f in $\mathbb{L}^2(\mathbb{R}^2)$ the corresponding scale-OS is within $\mathcal{W}_\psi(f) \in \mathbb{C}_K^{SIM(2)} \subset \mathbb{L}^2(SIM(2))$ and for any fixed $a \in (0, \infty)$, $\mathcal{W}_\psi(f)(\cdot, \cdot, a, \cdot) \in \mathbb{L}_2(SE(2))$. Let $\Phi_t : \mathbb{L}_2(SE(2)) \rightarrow \mathbb{L}_2(SE(2))$ denote nonlinear adaptive diffusion (CED-OS) on the $SE(2)$ group which is the solution operator of (57) at stopping time t . We propose the operator Λ on scale-OS defined as

$$(\Lambda[(\mathcal{W}_\psi f)])(x, y, a_i, \theta) = \sum_{i=1}^m (\Phi_{t_{a_i}}[\mathcal{W}_\psi f(\cdot, \cdot, a_i, \cdot)])(x, y, \theta), \quad (58)$$

where $(x, y, \theta) \in \mathbb{R}^2 \times [0, 2\pi)$ and $\{a_i\}_{i=1}^m$ is the discretization of $[a^-, a^+]$. Recall the definition of $0 < a^- < a^+ < \infty$ from Section 2.4. Here we make the specific choice of t_{a_i} with $t_{a_i} \leq t_{a_k}$ where $1 \leq i < k \leq m$.

The idea here is that on lower scales we have to diffuse more as noise is often dominant at lower scales and therefore lower scales need higher diffusion time.

4.3 Employing the gauge frames for differential invariany features - Vesselness

Retinal vasculature images are highly useful for non-invasive investigation of the quality of the vascular system which is affected in case of diseases such as (diabetic retinopathy, glaucoma, hypertension, arteriosclerosis, Alzheimers disease), see [57]. Here accurate and robust detection of the vascular tree is of vital importance [58, 59, 60, 61, 36]. The vascular tree structure in these retinal images is often hard to detect due to low-contrast, noise, the presence of tiny vessels, mirco-bleedings and other abnormalities due to diseases, bifurcations, crossings, occurring at multiple scales, and that is precisely where our continuous wavelet framework on $SIM(2)$ (i.e. multiple scale orientation scores) and the left-invariant evolutions acting upon them comes into play. In this section we will briefly show some benefits of our framework in terms of multi-scale vesselness filtering, see [62, 63], enhancement and tracking as illustrated in Figures 17 and 18. We would like to clarify that although $SIM(2)$ vesselness filter summarized below is based on the framework presented in this article, it was developed in [63] and has been presented here to demonstrate benefits.

Let $f : \mathbb{R}^2 \rightarrow \mathbb{R}$ be a greyscale image. Let $H^s f := G_s * (Hf)$ denote the Hessian of a Gaussian derivative at scale $s = \sigma^2/2$, with eigensystem $E_{\lambda_1} = \langle \mathbf{e}_1 \rangle$, $E_{\lambda_2} = \langle \mathbf{e}_2 \rangle$. Then the vesselness filter is given by

$$\mathcal{V}_{\sigma_1, \sigma_2}^{R, S}(f) = \begin{cases} e^{-\frac{R^2}{2\sigma_1^2}} \left(1 - e^{-\frac{S^2}{2\sigma_2^2}} \right) & \text{if } \lambda_2 > 0 \\ 0 & \text{if } \lambda_2 \leq 0 \end{cases}$$

with anisotropy measure $R = \lambda_1/\lambda_2$ and structureness $S = \lambda_1^2 + \lambda_2^2$. Typically $\sigma_1 = 1/2$ and $\sigma_2 = 0.2\|S\|_\infty$.

Now let us rewrite this filter in gauge derivatives $(\partial_\xi^s, \partial_\eta^s)$ where ∂_ξ^s takes the Gaussian derivative along \mathbf{e}_1 at scale $s = \sigma^2/2$ whereas ∂_η^s takes the Gaussian derivative along \mathbf{e}_2 at scale $s = \sigma^2/2$. Then the matrix representation of H^s w.r.t. local frame of reference becomes³

$$\mathcal{V}_{\sigma_1, \sigma_2}(f) = \begin{cases} e^{-\frac{1}{2\sigma_1^2} \left(\frac{f_{\eta\eta}^s}{f_{\xi\xi}^s} \right)} \left(1 - e^{-\frac{(f_{\eta\eta}^s)^2 + (f_{\xi\xi}^s)^2}{2\sigma_2^2}} \right) & \text{if } f_{\eta\eta} > 0 \\ 0 & \text{if } f_{\eta\eta} \leq 0. \end{cases}$$

Therefore on $SE(2)$ -CS transformed image where we have left-invariant frames $\{\partial_\xi, \partial_\eta, \partial_\theta\}$ with $\xi = x \cos \theta + y \sin \theta$, $\eta = -x \sin \theta + y \cos \theta$ we propose the vesselness filter on $SE(2)$ -CS transformed image $U := \mathcal{W}_\psi(f)$

$$\mathbf{x} \mapsto \frac{|\mathcal{V}_{\sigma_1, \sigma_2}(U(\cdot, \theta))|(\mathbf{x})}{\max_{(\mathbf{x}, \theta) \in SE(2)} |\mathcal{V}_{\sigma_1, \sigma_2}(U(\cdot, \theta))|(\mathbf{x})} \quad \text{with } \sigma_1 = \frac{1}{2}, \sigma_2 = 0.2 \max_x \Delta_x U(x, \theta) = 0.2\|S\|_\infty.$$

However, akin to the coherence enhancing diffusion on orientation scores [39] better results are obtained by using a local gauge frame $\{\partial_a^s, \partial_b^s, \partial_c^s\}$ defined in Eq. (56) with the best exponential curve fit (whose tangent c corresponds to the eigenvalue of 3D-Hessian $H_\beta^s U$ with smallest eigenvalue). In this case for all $g \in SE(2)$ we have

$$\tilde{\mathcal{V}}_{\sigma_1, \sigma_2}(U) = \begin{cases} e^{-\frac{1}{4\sigma_1^2} \frac{(U_{cc}^s)^2}{(U_{aa}^s + U_{bb}^s)^2}} \left(1 - e^{-\frac{(U_{aa}^s + U_{bb}^s)^2 + (U_{cc}^s)^2}{2\sigma_2^2}} \right) & \text{if } U_{aa}^s + U_{bb}^s > 0 \\ 0 & \text{if } U_{aa}^s + U_{bb}^s \leq 0. \end{cases} \quad (59)$$

Note that we again have anisotropy measure $R = \frac{2\lambda_1}{\lambda_2 + \lambda_3}$, structureness $S = \lambda_1^2 + \frac{(\lambda_2 + \lambda_3)^2}{2}$, $\sigma_1 = \frac{1}{2}$ and $\sigma_2 = 0.2\|U_{aa}^s + U_{bb}^s\|_\infty$. Then we normalize

$$(V_{\sigma_1, \sigma_2}(U))(g) = \frac{(\tilde{\mathcal{V}}_{\sigma_1, \sigma_2}(U))(g)}{\|\tilde{\mathcal{V}}_{\sigma_1, \sigma_2}(U)\|_\infty} \quad (60)$$

³Here f_y denotes partial derivative of f w.r.t. y .

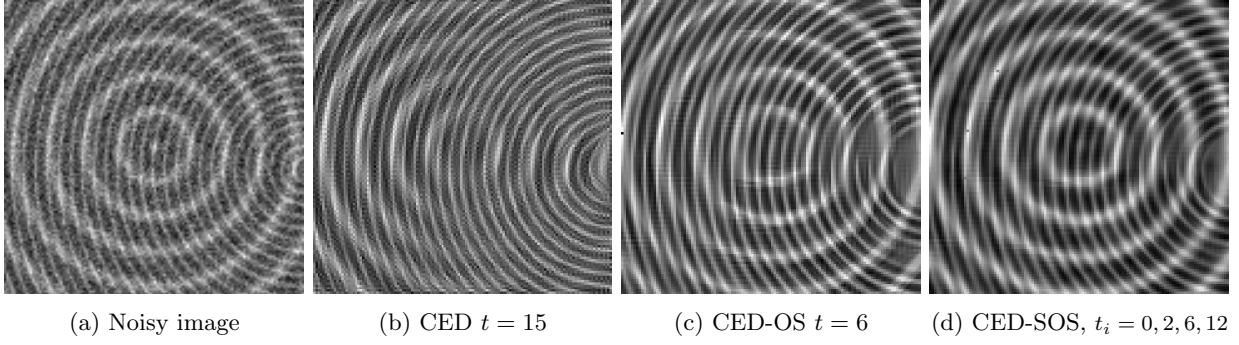


Figure 11: Comparison of CED [6], CED-OS [7] and our proposed method CED-SOS. In CED-SOS multi-scale crossing structures are better preserved. Observe that CED-OS and CED-SOS deal appropriately with crossings, unlike CED

to get the result of $SE(2)$ vesselness filter. Note that Gaussian derivatives in the score must be isotropic with scale $s > 0$ in the spatial part (in order to preserve the commutators of the generators during regularization) and $s = \beta^2$ in the angular part, for details see [63],[56, Ch.5].

Finally, when extending the framework to CW transformed image (multiple-scale OS) $(\mathcal{W}_\psi f)(x, y, \theta, a_l)$ with $a_l = \exp(ls_\rho)a_0$ we apply the $SE(2)$ vesselness filter on each scale layer $(\mathcal{W}_\psi f)(\cdot, \cdot, \cdot, a_l)$ with a_l fixed where we adapt $\sigma_2(a_l) = 0.1 \exp(ls_\rho) \|\mathcal{U}_f(\cdot, \cdot, \cdot, a_l)\|_\infty$.

5 Results

Parameters used for creating WT on images (scale orientation score): No. of scales = 4, No. of orientations = 20. The parameters that we used for CED are (for explanation of parameters see[6]): $\sigma = 0.5$, $\rho = 4$, $C = 1$ and $\alpha = 0.001$. The non-linear diffusion parameters for CED-OS and CED-SOS for each scale are: $\rho_s = 12$, $\tilde{\rho} = 1.5$, $\beta = 0.058$ and $c = 0.08$. All the experiments in this section use these parameters (unless otherwise indicated in the caption) and the varying end times are indicated below the images. We have enforced horizontality in the experiments involving CED-OS, see [7] for more details.

Figure 11 compares the effect of CED, CED-OS and CED-SOS on an artificial image containing additive superimposition of two images with concentric circles of varying widths. The new proposed method yields visually better results compared to both CED and CED-OS.

In Figure 12 we compare the proposed algorithm with state of the art denoising algorithms [64] on a noisy Lena image. We present comparisons with Non-local Means filter [65] and Iterative steering kernel regression [66] using standard parameter settings. Although our method is designed to deal with very noisy medical images containing crossing lines and various scales which differ from the Lena image, our method nonetheless performs very well compared to the state-of the art. In fact, our method shows better results in terms of robustness and higher noise levels, whereas the other methods show better results at lower noise levels. At the smaller noise levels further visual improvements of our method could be obtained by including median filtering techniques rather than diffusion techniques at large flat (isotropic) areas.

In Figure 13 we consider a typical example of a medical imaging application containing crossing lines at various scales in a low-contrast medical (2-photon microscopy) image for which we actually designed our algorithm. Note that these kind of images are acquired in tissue engineering research where the goal is to e.g. create artificial heart valves [67]. On these challenging type of images we obtain considerable improvements over the state of the art denoising algorithms as we appropriately deal with multiple scale crossings.

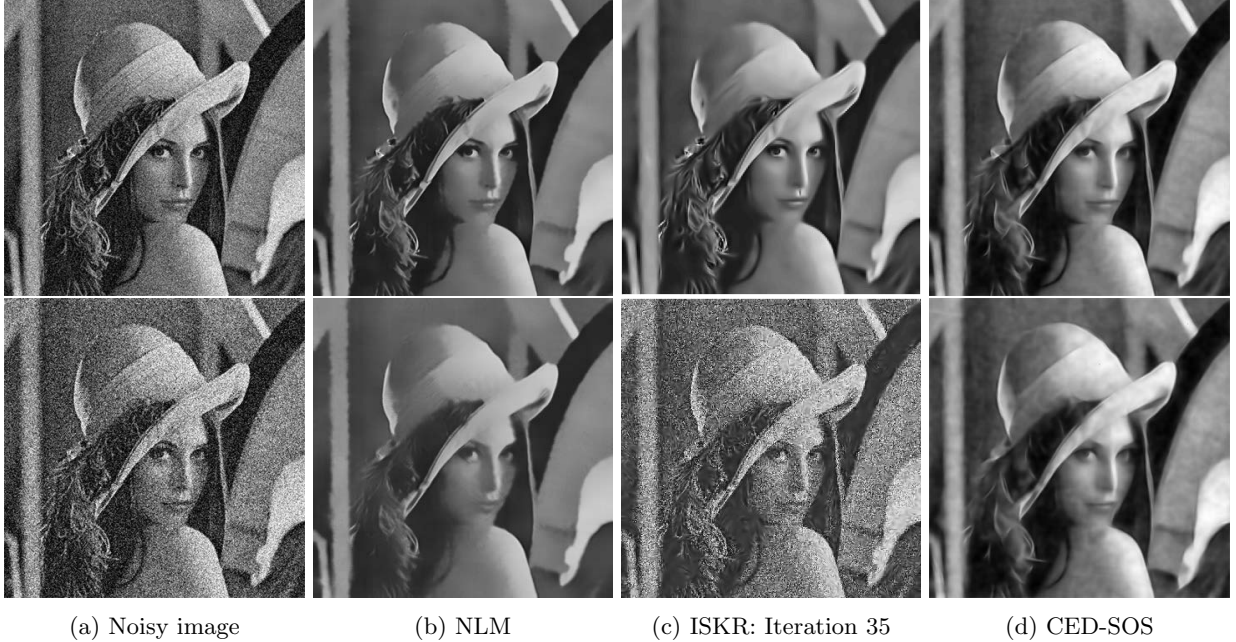


Figure 12: Comparison of CED-SOS with the state of the art denoising algorithms [64] with standard parameters on Lena image with gaussian noise (top: $\sigma = 35$, bottom: $\sigma = 60$). (a) Noisy input image (b) Non-local Means filter [65] (c) Iterative steering kernel regression [66] (d) CED-SOS, top: $t_i = 0, 2, 8, 9$, bottom: $t_i = 0, 2, 12, 14$.

Furthermore, to illustrate the potential of the currently proposed algorithm over previous works on crossing preserving diffusion and coherence enhancing diffusion we have included Figure 14.

For further comparison and in order to support the potential and wide applicability of our method in medical imaging, we also ran our algorithm on an image containing collagen fibers within bone tissue in Figure 15. Here the loss of small-scale data in CED-OS compared to CED-SOS is evident, an indeed a basic tracking algorithm (based on [34] involving thresholding $\partial_\eta^2 \mathcal{W}_\psi f$ and a basic morphological component method) reveals the benefit: “Tracking on CED-SOS outperforms tracking on CED-OS”, see Figure 16. On the other hand CED-OS has the advantage that it is faster and its implementation consumes far less memory (a factor in the order of the number of discrete scales).

In Figure 17 we show some first results of $SIM(2)$ vesselness-filter described in Section 4.3. These experiments illustrate that the $SIM(2)$ vesselness filter outperforms the multiple scale vesselness filtering acting directly in the image domain, as again no problems arise in areas with crossings/bifurcations. For further underpinning via qualitative comparisons on the HRF-benchmark sequence see [63]. Note that Figure 17 in addition to presenting the benefits of our continuous wavelet transform on $SIM(2)$ also shows the potential of including multiple scale crossing-preserving enhancements prior to the vesselness filtering (see Figure 17(d) where we have selected a problematic patch).

In Figure 18 we show the advantage of using $SIM(2)$ crossing preserving multi-scale enhancements CED-SOS prior to tracking retinal vessel via a state of the art tracking algorithm [36].

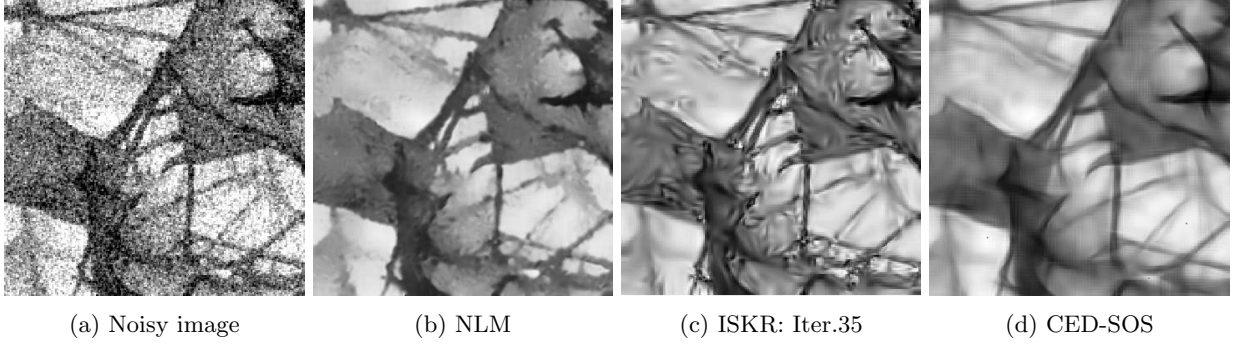


Figure 13: Comparison of CED-SOS with the state of the art denoising algorithms with standard parameters on a Collagen tissue from a cardiac wall. (a) Noisy input image (b) Non-local Means filter (c) Iterative steering kernel regression, Iteration-35 (d) CED-SOS

6 Conclusions

There are two different tasks achieved in this article.

1. Designing an invertible score on $SIM(2)$, which also allows for accurate and efficient implementation of subsequent enhancement by contextual flows.
2. Construction of contextual flows in the wavelet domain for the enhancement of elongated multi-scale crossing/bifurcating structures, via left-invariant PDEs on $SIM(2)$.

Regarding the first task we have presented a generalized unitarity result for algebraic affine Lie groups. This result is then used to design a multi-scale orientation score appropriate for subsequent left-invariant flows. For the second task we have shown that only left-invariant flows on multi-scale orientation scores (defined on $SIM(2)$) robustly relate to Euclidean invariant operations on images. Furthermore we have provided a differential-geometric and probabilistic interpretation of left-invariant PDEs on $SIM(2)$ which provides a strong intuitive rationale for the choice of left-invariant PDEs and involved diffusion parameters.

We have also derived analytic approximations of Green's function of linear diffusion on $SIM(2)$. Finally, we have presented crossing multiple-scale (curvature adaptive) flows via non-linear left-invariant diffusions on invertible scores. Our preliminary results indicate that including the notion of scale in the framework of invertible orientation scores indeed has advantages over existing PDE techniques (CED, CED-OS).

An interesting next step would be to include scale interactions in numerical implementation of non-linear diffusion on $SIM(2)$. Extending the framework of scattering operators on Lie groups (Mallat et al. [54, 55]) to connect scattering operators to PDEs on $SIM(2)$ is an interesting topic for future work.

Acknowledgements The authors would like to acknowledge Erik Bekkers (Technische Universiteit Eindhoven) for fruitful discussions and ideas regarding numerical implementation of scale orientation score and tracking method used to create Figure 16. The authors would like to thank Jiang Zhang (Technische Universiteit Eindhoven) and Julius Hannink for experiments to create Figure 18 and Figure 17 respectively. The authors would also like to thank the anonymous referees for valuable suggestions and comments.

A Proof of Theorem 1

For every $\Phi \in \mathbb{C}_K^G$ has a \mathcal{W}_ψ pre-image $f \in \mathbb{L}_2(\mathbb{R}^d)$, i.e. $f = (\mathcal{W}_\psi)^{-1}[\Phi]$ with

$$\|\Phi\|_{\mathbb{C}_K^G}^2 = (\Phi, \Phi)_{\mathbb{C}_K^G} = (f, f)_{\mathbb{L}_2(\mathbb{R}^d)} = \|f\|_{\mathbb{L}_2(\mathbb{R}^d)}^2.$$

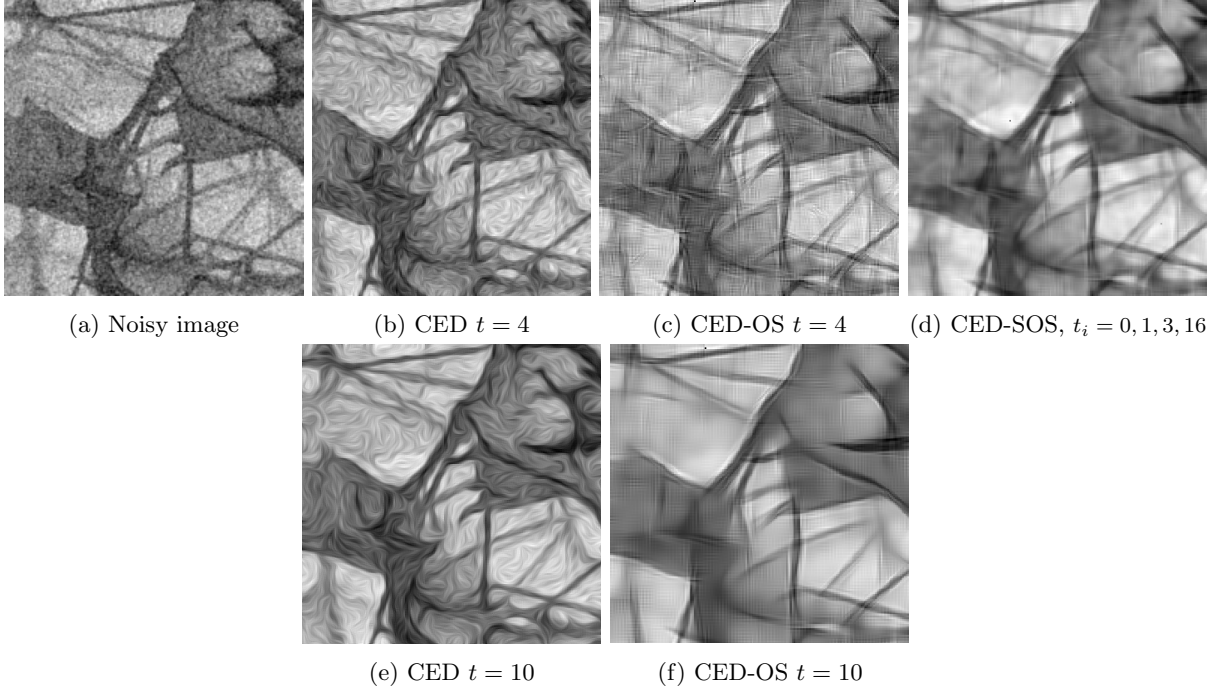


Figure 14: Results of CED, CED-OS and CED-SOS on a microscopy image of a Collagen tissue in the cardiac wall. CED-OS exhibits artefacts for small end time, see (c), which vanish if the algorithm is allowed to run longer at the cost of small-scale information, see (f). Therefore best visual results are obtained with CED-SOS.

We need to show that $\|\Phi\|_{\mathbb{C}_K^G}^2 = \|\Phi\|_{M_\psi}^2 := (\Phi, \Phi)_{M_\psi}^{\frac{1}{2}}$, where we recall (4) for the definition of the M_ψ -inner product. We have,

$$\int_{\mathbb{R}^d} |f(y)|^2 dy = \int_{\mathbb{R}^d} |\hat{f}(\omega)|^2 d\omega = \int_{\Omega} |\hat{f}(\omega)|^2 \frac{M_\psi(\omega)}{M_\psi(\omega)} d\omega = \int_{\Omega} |\hat{f}(\omega)|^2 \frac{M_\psi(\omega)}{M_\psi(\omega)} d\omega. \quad (61)$$

Recall that T is assumed to be a linear algebraic group (see [41] for definition) and therefore it has locally closed (dual) orbits. This leads to $\Omega_c = \Omega_{cr}$ in [34, Ch 5] and since Ω_{cr} is open, [34, Prop 5.7], we have that $\mu(\bar{\Omega} \setminus \Omega) = 0$, where μ is the usual Lebesgue measure on \mathbb{R}^d , giving us the final equality in (61). We can further write (61) as,

$$\begin{aligned} \int_{\mathbb{R}^d} |f(y)|^2 dy &= \int_{\Omega} |\hat{f}(\omega)|^2 \frac{1}{M_\psi(\omega)} \int_T \frac{|(\mathcal{F}\mathcal{R}_t\psi)(\omega)|^2}{\det(\tau(t))} d\mu_T(t) d\omega = \int_{\Omega} \left\{ \int_T \frac{\overline{\hat{f}(\omega)} (\mathcal{F}\mathcal{R}_t\psi(\omega)) \hat{f}(\omega) (\mathcal{F}\mathcal{R}_t\psi(\omega))}{\det(\tau(t))} \right\} \frac{d\omega}{M_\psi(\omega)} \\ &= \int_{\Omega} \int_T \overline{(\mathcal{F}\Phi(\cdot, t))(\omega)} (\mathcal{F}\Phi(\cdot, t))(\omega) d\mu_T(t) \frac{d\omega}{M_\psi(\omega)} = \int_{\Omega} \left(\int_T |\mathcal{F}\Phi(\cdot, t)(\omega)|^2 d\mu_T(t) \right) M_\psi^{-1}(\omega) d\omega. \end{aligned}$$

As a result $\Phi \in \mathbb{H}_\psi \otimes \mathbb{L}_2(T; \frac{d\mu_T(t)}{\det(\tau(t))})$ and we have,

$$(f, f)_{\mathbb{L}_2(\mathbb{R}^d)} = (\mathcal{W}_\psi f, \mathcal{W}_\psi f)_{\mathbb{C}_K^G} = \int_T \left(M_\psi^{-\frac{1}{2}} \mathcal{F}\Phi(\cdot, t), M_\psi^{-\frac{1}{2}} \mathcal{F}\Phi(\cdot, t) \right) d\mu_T(t),$$

from which the result follows. \square

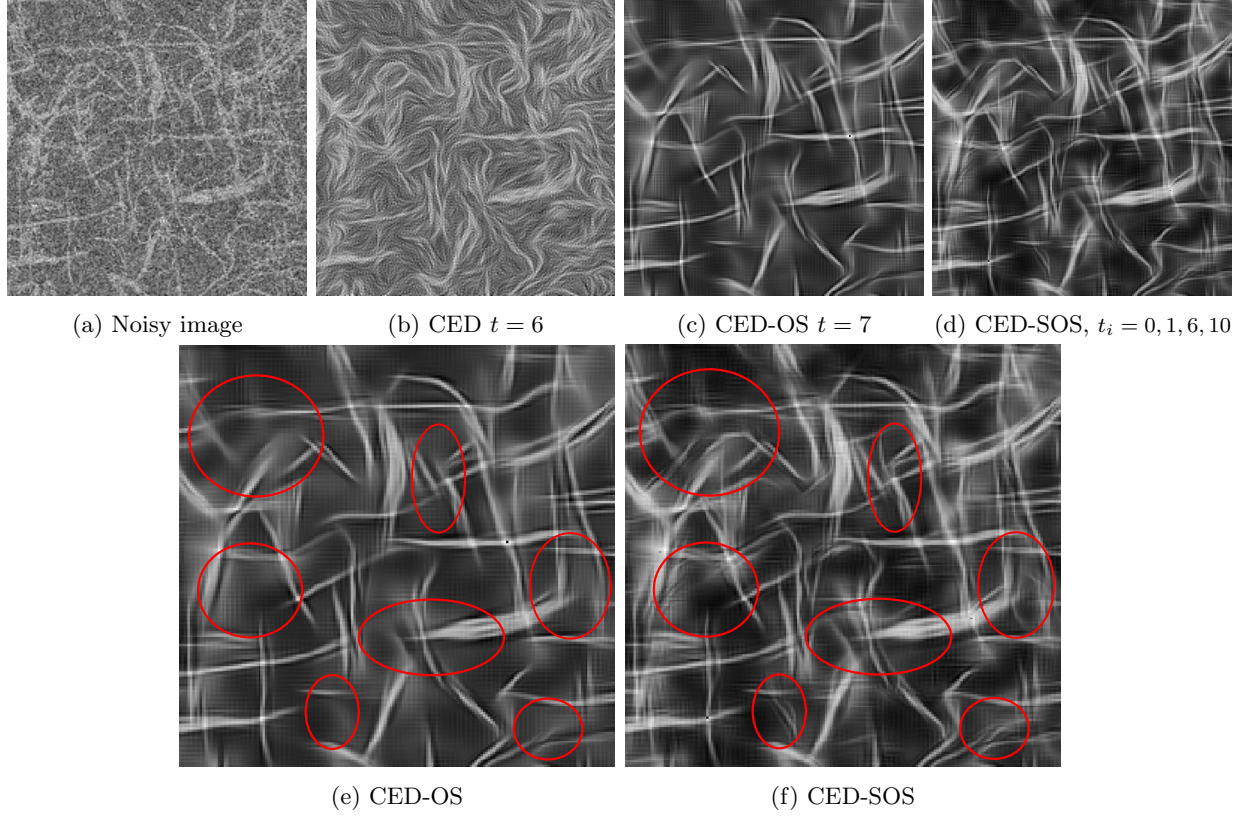


Figure 15: Top: Results of enhancement via of CED, CED-OS and CED-OS on Scale-OS on an image containing collagen fibres from a bone tissue. Bottom: Circled regions show loss of small-scale information in CED compared CED-SOS.

B Proof of Theorem 8

Note that since

$$\widetilde{\mathcal{W}}_\psi[\mathcal{U}_g[f]](h) = (\mathcal{U}_h\psi, \mathcal{U}_g f)_{\mathbb{L}_2(\mathbb{R}^d)} = (\mathcal{U}_{g^{-1}h}\psi, f)_{\mathbb{L}_2(\mathbb{R}^d)} = \mathcal{L}_g[\widetilde{\mathcal{W}}_\psi[f]](h)$$

we have

$$\widetilde{\mathcal{W}}_\psi \mathcal{U}_g = \mathcal{L}_g \widetilde{\mathcal{W}}_\psi, \text{ for all } g \in G. \quad (62)$$

Moreover,

$$(\widetilde{\mathcal{W}}_\psi \mathcal{U}_g f, U)_{\mathbb{L}_2(G)} = (\mathcal{L}_g \widetilde{\mathcal{W}}_\psi, U)_{\mathbb{L}_2(G)} \Leftrightarrow (f, \mathcal{U}_{g^{-1}}(\widetilde{\mathcal{W}}_\psi)^* U)_{\mathbb{L}_2(G)} = (f, (\widetilde{\mathcal{W}}_\psi)^* \mathcal{L}_{g^{-1}} U)_{\mathbb{L}_2(G)}$$

for all $U \in \mathbb{L}_2(G)$, $f \in \mathbb{L}_2(\mathbb{R}^d)$, $g \in G$ and therefore we have,

$$\mathcal{U}_g(\widetilde{\mathcal{W}}_\psi)^* = \mathcal{L}_g(\widetilde{\mathcal{W}}_\psi)^*, \text{ for all } g \in G. \quad (63)$$

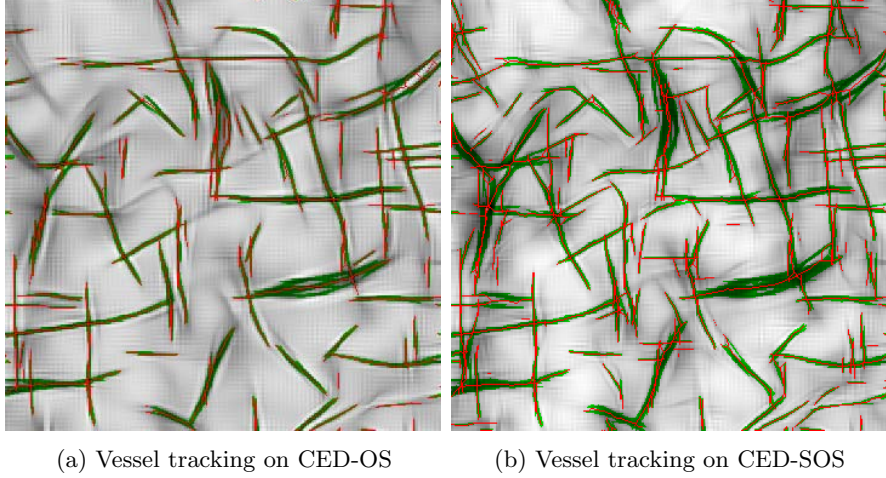


Figure 16: Results of a vessel tracking method [36] on the images enhanced by CED-OS and CED-SOS. As expected tracking on CED-SOS enhanced images give better results.

(Necessary condition) Assuming that $(\mathbb{P}_\psi \circ \Phi)$ is left invariant it follows from (30), (62) and (63) that

$$\begin{aligned}
\Upsilon[\mathcal{U}_g f] &= (\widetilde{\mathcal{W}}_\psi)^* \circ \Phi \circ \widetilde{\mathcal{W}}_\psi \circ \mathcal{U}_g[f] \\
&= (\widetilde{\mathcal{W}}_\psi)^* \circ (\mathbb{P}_\psi \circ \Phi) \circ \widetilde{\mathcal{W}}_\psi \circ \mathcal{U}_g[f] \\
&= (\widetilde{\mathcal{W}}_\psi)^* \circ (\mathbb{P}_\psi \circ \Phi) \circ \mathcal{L}_g \circ \widetilde{\mathcal{W}}_\psi[f] \\
&= (\widetilde{\mathcal{W}}_\psi)^* \circ \mathcal{L}_g \circ (\mathbb{P}_\psi \circ \Phi) \circ \widetilde{\mathcal{W}}_\psi[f] \\
&= \mathcal{U}_g \circ (\widetilde{\mathcal{W}}_\psi)^* \circ (\mathbb{P}_\psi \circ \Phi) \circ \widetilde{\mathcal{W}}_\psi[f] = \mathcal{U}_g[\Upsilon[f]]
\end{aligned} \tag{64}$$

for all $f \in \mathbb{L}_2(\mathbb{R}^2)$ and $g \in G$. Thus we have $\Upsilon \mathcal{U}_g = \mathcal{U}_g \Upsilon$ for all $g \in G$.

(Sufficient condition) Now suppose Υ is Euclidean invariant. Then again by (62) and (63) we have that,

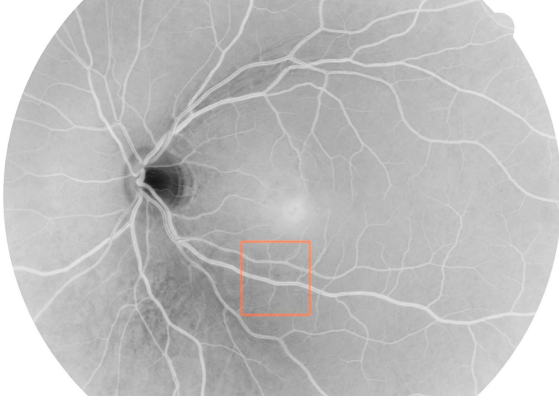
$$(\widetilde{\mathcal{W}}_\psi)^* \circ \Phi \circ \mathcal{L}_g \circ \widetilde{\mathcal{W}}_\psi[f] = (\widetilde{\mathcal{W}}_\psi)^* \circ \mathcal{L}_g \circ \Phi \circ \widetilde{\mathcal{W}}_\psi[f],$$

for all $f \in \mathbb{L}_2(\mathbb{R}^2)$ and $g \in G$. Since the range of $\mathcal{L}_g|_{\mathbb{C}_K^G}$ and the range of $(\mathbb{P}_\psi \circ \Phi)$ is contained in \mathbb{C}_K^G and since $(\widetilde{\mathcal{W}}_\psi)^*|_{\mathbb{C}_K^G} = (\mathcal{W}_\psi)^{-1}$, we have $(\mathbb{P}_\psi \circ \Phi) \circ \mathcal{L}_g \circ \widetilde{\mathcal{W}}_\psi = \mathcal{L}_g \circ (\mathbb{P}_\psi \circ \Phi) \circ \widetilde{\mathcal{W}}_\psi$. As the range of $\widetilde{\mathcal{W}}_\psi$ equals \mathbb{C}_K^G , we have, $\mathcal{L}_g \circ (\mathbb{P}_\psi \circ \Phi) = (\mathbb{P}_\psi \circ \Phi) \circ \mathcal{L}_g$ for all $g \in G$.

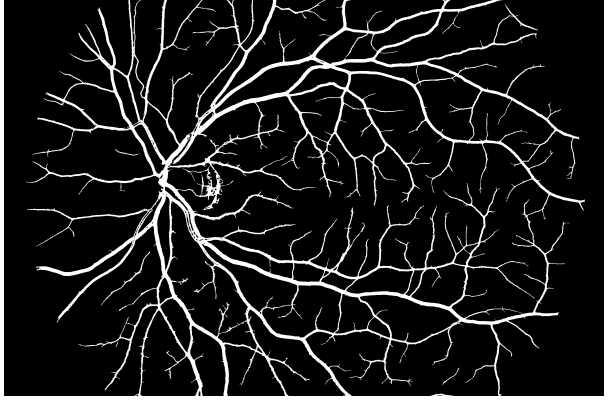
C Explicit formulation of exponential and logarithm curves

The exponential curves $g_0 \gamma_c(t) = (x(t), y(t), \tau(t), \theta(t))$ passing through $g_0 = (x_0, y_0, e^{\tau_0}, \theta_0)$ at $t = 0$ is,

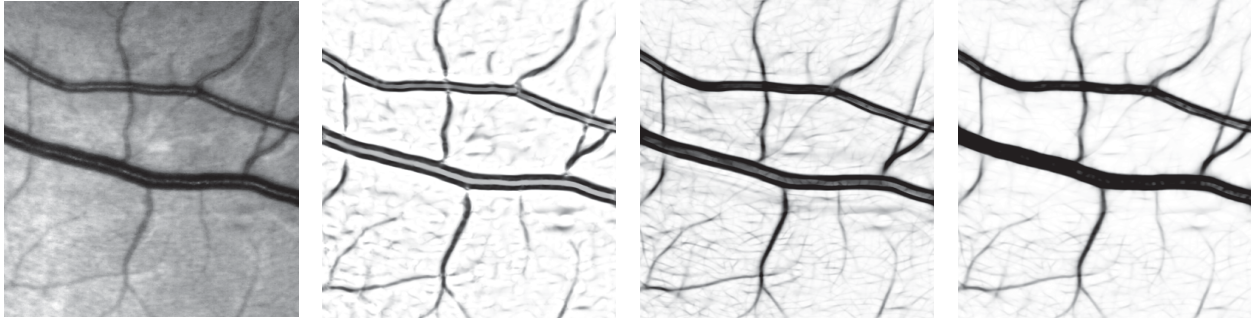
$$\begin{aligned}
x(t) &= \frac{1}{c_1^2 + c_4^2} [e^{\tau_0} c_1 ((-\sin[\theta_0] + e^{tc_4} \sin[tc_1 + \theta_0]) c_2 + (-\cos[\theta_0] + e^{tc_4} \cos[tc_1 + \theta_0]) c_3) + c_1^2 x_0 + \\
&\quad c_4 (e^{\tau_0} (-\cos[\theta_0] + e^{tc_4} \cos[tc_1 + \theta_0]) c_2 + e^{\tau_0} (\sin[\theta_0] - e^{tc_4} \sin[tc_1 + \theta_0]) c_3 + c_4 x_0)] \\
y(t) &= \frac{1}{c_1^2 + c_4^2} [e^{\tau_0} c_1 ((\cos[\theta_0] - e^{tc_4} \cos[tc_1 + \theta_0]) c_2 + (-\sin[\theta_0] + e^{tc_4} \sin[tc_1 + \theta_0]) c_3) + c_1^2 y_0 + \\
&\quad c_4 (e^{\tau_0} (-\sin[\theta_0] + e^{tc_4} \sin[tc_1 + \theta_0]) c_2 + e^{\tau_0} (-\cos[\theta_0] + e^{tc_4} \cos[tc_1 + \theta_0]) c_3 + c_4 y_0)] \\
\tau(t) &= tc_4 + \tau_0 \\
\theta(t) &= tc_1 + \theta_0.
\end{aligned} \tag{65}$$



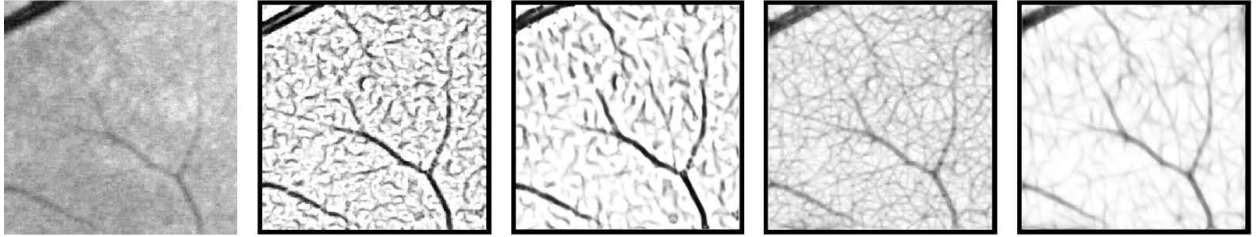
(a) Optical image of the retina where bloodvessels depart from the optic disk



(b) Segemented image via morphological components [63] based on the $SIM(2)$ vesselness filter.



(c) Comparison of vesselness filters. Left to Right: fragment of retinal image; Frangi vesselness filter [62] on image; $SIM(2)$ vesselness filter with frame $\partial_\theta, \partial_\xi, \partial_\eta, (\partial_\tau)$; $SIM(2)$ vesselness filter with gauge frame $\partial_a, \partial_b, \partial_c, (\partial_\tau)$, see Eq.(59).



(d) Comparison of vesselness filters on a tough retinal image patch with/without enhancements. Left to Right: typical fragment of retinal image where vesselness with standard parameters for the entire image fails; Frangi vesselness filter; Frangi vesselness filter after pre-enhancement via CED-SOS; $SIM(2)$ vesselness filter; $SIM(2)$ vesselness filter after pre-enhancement via CED-SOS.

Figure 17: Figures (b) shows the result of $SIM(2)$ vesselness (Sec.4.3) on an entire retinal fundus image (HRF database). See [63] for details. Figure (c) shows the advantage of $SIM(2)$ vesselness over commonly used Frangi approach. Figure (d) shows the advantage of enhancing the image prior to applying vesselness filters.

To explicitly determine the log map, we solve for $\{c^1, c^2, c^3, c^4\}$ from the equality, $g = \exp\left(t \sum_{i=1}^4 c^i A_i\right)$, where $g \in SIM(2)$ and c^i 's are as defined earlier. This is achieved by substituting $g_0 = e$, i.e. $x_0 = y_0 = \theta_0 = \tau_0 = 0$,

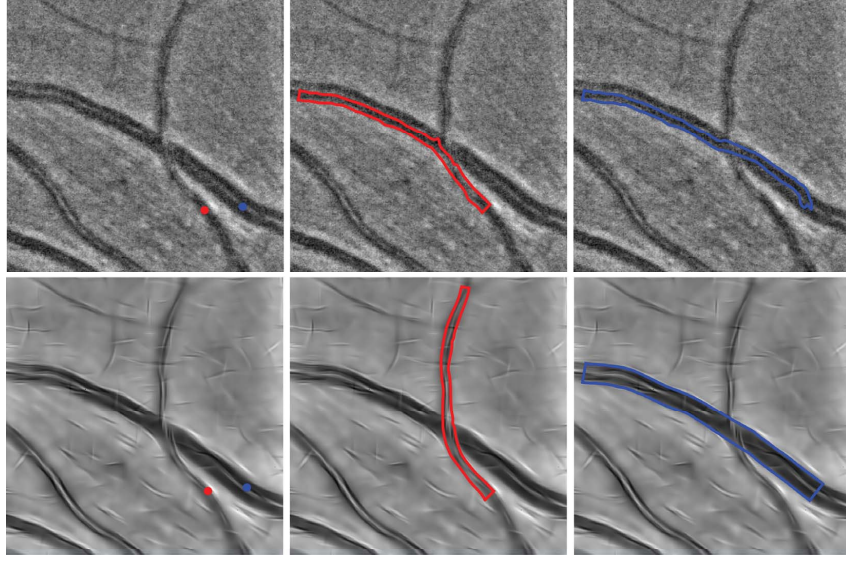


Figure 18: Advantage of $SIM(2)$ crossing preserving multi-scale enhancement in the tracking of retinal vessels via state of the art tracking algorithm [36]. Top: Tracking applied to original image data fails due to noise. Bottom: Tracking applied after enhancement via CED-SOS is successful.

in (65) yielding,

$$c^1 = \theta/t, \quad c^2 = \frac{(y\theta - x\tau) + (-\theta\eta + \tau\xi)}{t(1 + e^{2\tau} - 2e^\tau \cos \theta)}, \quad c^3 = \frac{-(x\theta + y\tau) + (\theta\xi + \tau\eta)}{t(1 + e^{2\tau} - 2e^\tau \cos \theta)}, \quad c^4 = \tau/t, \quad (66)$$

where we have made use of the definition of ξ and η ,

$$\xi = e^\tau(x \cos \theta + y \sin \theta), \quad \eta = e^\tau(-x \sin \theta + y \cos \theta).$$

D Proof of Theorem 10

We first note that, $U \in \mathcal{D}(d\mathcal{R}(A)) \Rightarrow (d\mathcal{R}(A)U) \in H$, where $H = \mathbb{L}_2(SIM(2))$. Then, $\mathcal{R}_{e^{tA}}U \in \mathcal{D}(d\mathcal{R}(A))$ follows as $[d\mathcal{R}(A)\mathcal{R}_{e^{tA}}](U) = [\mathcal{R}_{e^{tA}}d\mathcal{R}(A)](U)$, for all $U \in \mathcal{D}(d\mathcal{R}(A))$.

$$\begin{aligned} [d\mathcal{R}(A)\mathcal{R}_{e^{tA}}](U)(g) &= \left[\lim_{h \rightarrow 0} \frac{\mathcal{R}_{e^{hA}} - I}{h} \right] (\mathcal{R}_{e^{tA}}U)(g) = \lim_{h \rightarrow 0} \frac{\mathcal{R}_{e^{hA}}\mathcal{R}_{e^{tA}}(U(g)) - \mathcal{R}_{e^{tA}}(U(g))}{h} \\ &= \lim_{h \rightarrow 0} \frac{\mathcal{R}_{e^{tA}}\mathcal{R}_{e^{hA}}(U(g)) - \mathcal{R}_{e^{tA}}(U(g))}{h} = [\mathcal{R}_{e^{tA}}d\mathcal{R}(A)](U)(g), \end{aligned}$$

where we have used $\mathcal{R}_h(U(g)) = U(gh)$ and $e^{tA}e^{hA} = e^{(t+h)A} = e^{hA}e^{tA}$. This proves (1). We need to prove that $e^{td\mathcal{R}(A)}U = \mathcal{R}_{e^{tA}}U$, where $U \in \mathcal{D}(d\mathcal{R}(A))$, for all $A \in T_e(G)$, for all $t > 0$. By definition $e^{td\mathcal{R}(A)}U$ is the (strong) solution for $\frac{\partial W}{\partial t}(\cdot, t) = d\mathcal{R}(A)W(\cdot, t)$ with $W(g, 0) = U$. Now $\frac{\partial(\mathcal{R}_{e^{tA}}U)}{\partial t} = d\mathcal{R}(A)(\mathcal{R}_{e^{tA}}U)$, follows from,

$$\begin{aligned} \frac{\partial(\mathcal{R}_{e^{tA}}U)}{\partial t} &= \lim_{h \rightarrow 0} \frac{\mathcal{R}_{e^{(t+h)A}}U - \mathcal{R}_{e^{tA}}U}{h} = \lim_{h \rightarrow 0} \frac{\mathcal{R}_{e^{hA}}\mathcal{R}_{e^{tA}}U - \mathcal{R}_{e^{tA}}U}{h} \\ &= \lim_{h \rightarrow 0} \left[\left(\frac{\mathcal{R}_{e^{hA}} - I}{h} \right) \mathcal{R}_{e^{tA}}U \right] = d\mathcal{R}(A)(\mathcal{R}_{e^{tA}}U). \end{aligned} \quad (67)$$

Note that the limit used above is defined on the space $H = \mathbb{L}_2(SIM(2))$.

Let $d\mathcal{R}(A) = \mathcal{A} = \sum_{i=1}^4 c^i \mathcal{A}_i$. Then the solution for (41) is, $W(\cdot, t) = e^{-td\mathcal{R}(A)}U = \mathcal{R}_{e^{-tA}}U$, where the second equality follows from (2). Thus we have,

$$W(g, t) = U(ge^{-tA}) \quad \forall g \in SIM(2), \quad \forall t > 0 \Rightarrow W(g_0 e^{tA}, t) = U(g_0) \quad \forall t > 0. \quad (68)$$

From which the result follows. \square

E Approximation of $SIM(2)$ by a Nilpotent Group via Contraction

Following the general framework by ter Elst and Robinson [53], which involves semigroups on Lie groups generated by subcoercive operators, we consider a particular case by setting the Hilbert space $H = \mathbb{L}_2(SIM(2))$, the group $G = SIM(2)$ and the right-regular representation \mathcal{R} . Furthermore we consider the algebraic basis $\{\mathcal{A}_1 = \partial_\theta, \mathcal{A}_2 = \partial_\xi, \mathcal{A}_4 = \partial_\tau\}$ leading to the following filtration of the Lie algebra

$$\mathfrak{g}_1 := \text{span}\{\mathcal{A}_1, \mathcal{A}_2, \mathcal{A}_4\} \subset \mathfrak{g}_2 = [\mathfrak{g}_1, \mathfrak{g}_1] = \text{span}\{\mathcal{A}_1, \mathcal{A}_2, \mathcal{A}_3, \mathcal{A}_4\} = \mathcal{L}(SIM(2)). \quad (69)$$

Based on this filtration we assign the following weights to the generators:

$$w_1 = w_2 = w_4 = 1 \text{ and } w_3 = 2. \quad (70)$$

For e.g. $w_2 = 1$ since \mathcal{A}_2 occurs first in \mathfrak{g}_1 , while $w(3) = 2$ since \mathcal{A}_3 occurs in \mathfrak{g}_2 and not \mathfrak{g}_1 . Based on these weights we define the following dilations on the Lie algebra $T_e(SIM(2))$ (recall $A_i = \mathcal{A}_i|_e$),

$$\begin{aligned} \gamma_q \left(\sum_{i=1}^4 c^i A_i \right) &= \sum_{i=1}^4 q^{w_i} c^i A_i, \quad \forall c^i \in \mathbb{R}, \\ \tilde{\gamma}_q(x, y, \tau, \theta) &= \left(\frac{x}{q^{w_2}}, \frac{y}{q^{w_3}}, \frac{\tau}{q^{w_4}}, e^{i \frac{\theta}{q^{w_1}}} \right), \end{aligned}$$

with the weights w_i defined in (70), and for $0 < q \leq 1$ we define the Lie product $[A, B]_q = \gamma_q^{-1}[\gamma_q(A), \gamma_q(B)]$. Let $(SIM(2))_t$ be the simply connected Lie group generated by the Lie algebra⁴ $(T_e(SIM(2)), [\cdot, \cdot]_q)$. The group products on these intermediate groups $(SIM(2))_{q \in (0, 1]}$ are given by,

$$(x, y, \tau, \theta) \cdot_q (x', y', \tau', \theta') = (x + e^{\tau q} [\cos(q\theta)x' - q \sin(q\theta)y'], y + e^{\tau q} [\frac{\sin(q\theta)}{q} x' + \cos(q\theta)y'], \tau + \tau', \theta + \theta'). \quad (71)$$

The dilation on the Lie algebra coincides with the pushforward of the dilation on the group $\gamma_q = (\tilde{\gamma}_q)_*$ and therefore the left-invariant vector fields on $(SIM(2))_t$ are given by

$$\mathcal{A}_i^q|_g = (\tilde{\gamma}_q^{-1} \circ L_g \circ \tilde{\gamma}_q)_* A_i,$$

for all $q \in (0, 1]$ which leads to,

$$\begin{aligned} \mathcal{A}_i^q|_g \phi &= (\tilde{\gamma}_q^{-1} \circ L_g)_* (\tilde{\gamma}_q)_* A_i \phi = (\tilde{\gamma}_q^{-1} \circ L_g)_* (\gamma_q)(A_i) \phi = t^{w_i} (\tilde{\gamma}_q^{-1} \circ L_g)_* (A_i) \phi \\ &= q^{w_i} (\tilde{\gamma}_q^{-1})_* \mathcal{A}_i|_g \phi = q^{w_i} \mathcal{A}_i|_{\tilde{\gamma}_q^{-1} g} (\phi \circ \tilde{\gamma}_q), \end{aligned}$$

⁴Note that $(SIM(2))_q = \exp_q(T_e(SIM(2)))$.

for all smooth complex valued functions ϕ defined on a open neighbourhood around $g \in SIM(2)$. So for all $g = (x, y, \tau, \theta) \in SIM(3)$ we have,

$$\begin{aligned}\mathcal{A}_1^t|_g &= q\left(\frac{1}{q}\partial_\theta\right) = \partial_\theta \\ \mathcal{A}_2^q|_g &= q\left[e^{\tau q}\left(\frac{\cos(q\theta)}{q}\partial_x + \frac{\sin(q\theta)}{q^2}\partial_y\right)\right] = e^{\tau q}\left(\cos(q\theta)\partial_x + \frac{\sin(q\theta)}{q}\partial_y\right) \\ \mathcal{A}_3^q|_g &= q^2\left[e^{\tau q}\left(-\frac{\sin(q\theta)}{q}\partial_x + \frac{\cos(q\theta)}{q^2}\partial_y\right)\right] = e^{\tau q}(-q\sin(q\theta)\partial_x + \cos(q\theta)\partial_y) \\ \mathcal{A}_4^q|_g &= \partial_\tau.\end{aligned}\tag{72}$$

Furthermore, $[A_i, A_j]_q = \gamma_q^{-1}[\gamma_q(A_i), \gamma_q(A_j)] = \gamma_q^{-1}q^{w_i+w_j}[A_i, A_j] = \sum_{k=1}^4 q^{w_i+w_j-w_k}c_{ij}^k A_k$ and therefore

$$[A_1, A_2]_q = A_3, \quad [A_1, A_3]_q = -q^2 A_2, \quad [A_4, A_2]_q = q A_2, \quad [A_4, A_3]_q = q A_3.\tag{73}$$

Analogously to the case $q = 1$, $(SIM(2))_{q=1} = SIM(2)$, there exists an isomorphism of the Lie algebra at the unity element $T_e((SIM(2))_q)$ and the left-invariant vector fields on the group $\mathcal{L}((SIM(2))_q)$:

$$(A_i \leftrightarrow \mathcal{A}_i^q \text{ and } A_j \leftrightarrow \mathcal{A}_j^q) \Rightarrow [A_i, A_j]_q \leftrightarrow [\mathcal{A}_i^q, \mathcal{A}_j^q].\tag{74}$$

It can be verified that the left invariant vector fields \mathcal{A}_i^q satisfy the same commutation relations as (73). In the case $H \equiv \lim_{q \downarrow 0} (SIM(2))_q$ the left-invariant vector fields are given by

$$\mathcal{A}_1^0 = \partial_\theta, \quad \mathcal{A}_2^0 = \partial_x + \theta \partial_y, \quad \mathcal{A}_3^0 = \partial_y, \quad \mathcal{A}_4^0 = \partial_\tau.\tag{75}$$

So, the homogeneous nilpotent contraction Lie group equals

$$H_3 = \lim_{q \downarrow 0} (SIM(2))_q \text{ and } SIM(2) = (SIM(2))_{q=1}/(\{0\} \times \{0\} \times \{0\} \times 2\pi\mathbb{Z}),\tag{76}$$

with the Lie algebra $\mathcal{L}(H) = \text{span}\{\partial_\theta, \partial_x + \theta \partial_y, \partial_y, \partial_\tau\}$ and $\mathcal{L}(SIM(2)) = \text{span}\{\partial_\theta, \partial_\xi, \partial_\eta, \partial_\tau\}$.

F Differential-geometric interpretation of Left-invariant Evolutions

In order to keep track of orthogonality and parallel transport in such diffusions we need an invariant first fundamental form \mathcal{G} on $SIM(2)$, rather than the trivial, bi-invariant (i.e. left and right invariant), first fundamental form on $(\mathbb{R}^4, T(\mathbb{R}^4))$, where each tangent space $T_{\mathbf{x}(\mathbb{R}^4)}$ is identified with $T_0(\mathbb{R}^4)$ by standard parallel transport on \mathbb{R}^4 , i.e. $\mathcal{G}_{\mathbb{R}^4}(\mathbf{x}, \mathbf{y}) = \mathbf{x} \cdot \mathbf{y} = x^1 y^1 + x^2 y^2 + x^3 y^3 + x^4 y^4$.

Recall Theorem 8 which essentially states that operators Φ on scale-OS should be left-invariant (i.e. $\mathcal{L}_g \circ \Phi = \Phi \circ \mathcal{L}_g$) and not right-invariant in order to ensure that the effective operator Υ_ψ on the image is a Euclidean invariant operator. This suggests that the first fundamental form required for our diffusions on $SIM(2)$ should be left-invariant. The following theorem characterizes the formulation of a left-invariant first fundamental form w.r.t the $SIM(2)$ group.

Theorem 14 *The only real valued left-invariant (symmetric, positive, semidefinite) first fundamental form $\mathcal{G} : SIM(2) \times T(SIM(2)) \times T(SIM(2)) \rightarrow \mathbb{C}$ on $SIM(2)$ are given by,*

$$\mathcal{G} = \sum_{i=1}^4 \sum_{j=1}^4 g_{ij} \omega^i \otimes \omega^j, \quad g_{ij} \in \mathbb{R}.\tag{77}$$

where the dual basis $\{\omega^1, \omega^2, \omega^3, \omega^4\} \subset (\mathcal{L}(\text{SIM}(2)))^*$ of the dual space $(\mathcal{L}(\text{SIM}(2)))^*$ of the vector space $\mathcal{L}(\text{SIM}(2))$ of left-invariant vector fields spanned by

$$\{\mathcal{A}_1, \mathcal{A}_2, \mathcal{A}_3, \mathcal{A}_4\} = \{\partial_\theta, e^\tau(\cos \theta \partial_x + \sin \theta \partial_y), e^\tau(-\sin \theta \partial_x + \cos \theta \partial_y), \partial_\tau\}, \quad (78)$$

obtained by applying the operator $d\mathcal{R} : T_e(G) \rightarrow \mathcal{L}(G)$, defined as

$$(d\mathcal{R}(A)\phi)(g) = \lim_{t \downarrow 0} \frac{(\mathcal{R}_{\exp(tA)}\phi)(g) - \phi(g)}{t}, \quad A \in T_e(G), \phi \in \mathbb{L}_2(G), g \in G, \quad (79)$$

to the standard basis in the Lie algebra

$$\{A_1, A_2, A_3, A_4\} = \{\partial_\theta, \partial_x, \partial_y, \partial_a\} \subset T_e(\text{SIM}(2)), \quad (80)$$

is given by

$$\{\omega^1, \omega^2, \omega^3, \omega^4\} = \{d\theta, \frac{1}{e^\tau}(\cos \theta dx + \sin \theta dy), \frac{1}{e^\tau}(-\sin \theta dx + \cos \theta dy), d\tau\}. \quad (81)$$

The proof, see [68] for details, is similar to the $SE(2)$ case [39].

We consider the Maurer-Cartan form on $\text{SIM}(2)$ (discussed in the remainder of the subsection) and impose the following left-invariant, first fundamental form $\mathcal{G}_\beta : \text{SIM}(2) \times T(\text{SIM}(2)) \times T(\text{SIM}(2)) \rightarrow \mathcal{C}$ on $\text{SIM}(2)$,

$$\mathcal{G} = \sum_{i=1}^4 \sum_{j=1}^4 g_{ij} \omega^i \otimes \omega^j = \alpha^2 \omega^1 \otimes \omega^1 + \beta^2 \omega^2 \otimes \omega^2 + \beta^2 \omega^3 \otimes \omega^3 + \sigma^2 \omega^4 \otimes \omega^4. \quad (82)$$

Here σ tunes the cost of changing scale, β the cost of moving spatially and α the cost of moving angularly. By homogeneity we set $\alpha = 1$, as it is only $\frac{\beta}{\alpha}, \frac{\sigma}{\alpha}$ that matter. In order to understand the meaning of the next two theorems we need some definitions from differential geometry. See [69] for more details on these concepts.

Definition 15 Let M be a smooth manifold and G be a Lie group. A principle fiber bundle $P_G := (P, M, \pi, R)$ above a manifold M with structure group G is a tuple (P, M, π, R) such that P is a smooth manifold (called the total space of the principle bundle), $\pi : P \rightarrow M$ is a smooth projection map with $\pi(P) = M$ and $\pi(u \cdot a) = \pi(u)$, $\forall u \in P, a \in G$, R a smooth right action $R_g p = p \cdot g$, $p \in P, g, h \in G$. Finally it should satisfy the "local triviality" condition: For each $p \in P$ there is a neighbourhood U of p and a diffeomorphism $t : \pi^{-1}(U) \rightarrow U \times G$ of the form $t(u) = (\pi(u), \phi(u))$ where ϕ satisfies $\phi(u \cdot a) = \phi(u)a$ where the latter product is in G .

Definition 16 A principle fiber bundle $P_G := (P, M, \pi, R)$ is commonly equipped with a Cartan-Ehresmann connection form ω . This by definition is a Lie algebra $T_e(G)$ -valued 1-form $\omega : P \times T(P) \rightarrow T_e(G)$ on P such that

$$\begin{aligned} \omega(d\mathcal{R}(A)) &= A \text{ for all } A \in T_e(G) \\ \omega((R_h)_* A) &= \text{Ad}(h^{-1})\omega(A) \text{ for all vector fields } A \text{ in } G. \end{aligned} \quad (83)$$

It is also common practice to relate principle fiber bundles to vector bundles. Here one uses an external representation $\rho : G \rightarrow F$ into a finite-dimensional vector space F of the structure group to put an appropriate vector space structure on the fibers $\{\pi^{-1}(m) \mid m \in M\}$ in the principle fiber bundles.

Definition 17 Let P be a principle fiber bundle with finite dimensional structure group G . Let $\rho : G \rightarrow F$ be a representation in a finite-dimensional vector space F . Then the associated vector bundle is denoted by $P \times_\rho F$ and equals the orbit space under the right action

$$(P \times F) \times G \rightarrow P \times F \text{ given by } ((u, X), g) \mapsto (ug, \rho(g)X),$$

for all $g \in G, X \in F$ and $u \in P$.

Remark 18 $GL(T_e(SIM(2)))$ denotes the collection of linear operators on the Lie algebra $T_e(SIM(2))$. Note that each linear operator $\overline{Q} \in GL(T_e(SIM(2)))$ on $T_e(SIM(2))$ is 1-to-1 related to bilinear form Q on $(T_e(SIM(2)))^* \times T_e(SIM(2))$ by means of

$$\langle B, \overline{Q}A \rangle = Q(B, A), \text{ for all } B \in (T_e(SIM(2)))^*, A \in T_e(SIM(2)) \text{ and } \overline{Q} = \sum_{i=1}^4 Q(\omega^i|_e, \cdot) A_i.$$

So a basis for $GL(T_e(SIM(2)))$ is given by $\{\overline{\omega^i|_e \otimes A_j} \mid i, j \in \{1, 2, 3, 4\}\}$. For the simplicity of notation we omit the overline and write $\omega^i|_e \otimes A_j$ as it is clear from context whether we mean the bilinear form or the linear mapping.

Theorem 19 The Maurer-Cartan form ω on $SIM(2)$ can be formulated as

$$\omega_g(X_g) = \sum_{i=1}^4 \langle \omega^i|_g, X_g \rangle A_i, \quad X_g \in T_g(SIM(2)), \quad (84)$$

where $\{\omega^i\}_{i=1}^4$ is given by (81) and $A_i = \mathcal{A}_i|_e$; recall (78). It is a Cartan-Ehresmann connection form on the principle fiber bundle $P = (SIM(2), e, SIM(2), \mathcal{L}(SIM(2)))$, where $\pi(g) = e$, $R_g u = ug$, $u, g \in SIM(2)$. Let Ad denote the adjoint action of $SIM(2)$ on its own Lie algebra $T_e(SIM(2))$, i.e. $Ad(g) = (R_{g^{-1}} L_g)_*$, i.e. the push-forward of conjugation. Then the adjoint representation of $SIM(2)$ on the vector space $\mathcal{L}(SIM(2))$ of left-invariant vector-fields is given by

$$\widetilde{Ad}(g) = d\mathcal{R} \circ Ad(g) \circ \omega. \quad (85)$$

The adjoint representation gives rise to the associated vector bundle $SIM(2) \times_{\widetilde{Ad}} \mathcal{L}(SIM(2))$. The corresponding connecting form on this vector bundle is given by

$$\tilde{\omega} = \mathcal{A}_2 \otimes \omega^3 \wedge \omega^1 + \mathcal{A}_3 \otimes \omega^1 \wedge \omega^2 + \mathcal{A}_2 \otimes \omega^4 \wedge \omega^2 + \mathcal{A}_3 \otimes \omega^4 \wedge \omega^3. \quad (86)$$

Then $\tilde{\omega}$ yields the following 4×4 matrix-valued 1-form:

$$\tilde{\omega}_j^k(\cdot) := -\tilde{\omega}(\omega^k, \cdot, \mathcal{A}_j), \quad k, j \in \{1, 2, 3, 4\} \quad (87)$$

on the frame bundle, where the sections are moving frames⁵. Let $\{\mu_k\}_{k=1}^4$ denote the sections in the tangent bundle $E := (SIM(2), T(SIM(2)))$ which coincides with the left-invariant vector fields $\{\mathcal{A}_k\}_{k=1}^4$. Then the matrix-valued 1-form (78) yields the Cartan connection⁶ D on the tangent bundle $(SIM(2), T(SIM(2)))$ given by the covariant derivatives

$$\begin{aligned} D_{X|_{\gamma(t)}}(\mu(\gamma(t))) &:= D(\mu(\gamma(t)))(X|_{\gamma(t)}) \\ &= \sum_{k=1}^4 \dot{a}^k \mu_k(\gamma(t)) + \sum_{k=1}^4 a^k(\gamma(t)) \sum_{k=1}^4 \tilde{\omega}_k^j(X|_{\gamma(t)}) \mu_j(\gamma(t)) \\ &= \sum_{k=1}^4 \dot{a}^k \mu_k(\gamma(t)) + \sum_{k=1}^4 \dot{\gamma}^i(t) a^k(\gamma(t)) \Gamma_{ik}^j \mu_j(\gamma(t)), \end{aligned} \quad (88)$$

with $\dot{a}^k = \dot{\gamma}^i(t) (\mathcal{A}_i|_{\gamma(t)} a^k)$, for all tangent vectors $X|_{\gamma(t)} = \dot{\gamma}^i(t) \mathcal{A}_i|_{\gamma(t)}$ along a curve $t \mapsto \gamma(t) \in SIM(2)$ and all sections $\mu(\gamma(t)) = \sum_{k=1}^4 a^k(\gamma(t)) \mu_k(\gamma(t))$. The Christoffel symbols in (88) are constant $\Gamma_{ik}^j = -c_{ik}^j$, with c_{ik}^j the structure constants of the Lie algebra $T_e(SIM(2))$.

⁵See [69, Ch.8] for more details on frame bundles and moving frames.

⁶Following the definitions in [69], formally this is not a Cartan connection but a Koszul connection, see [69, Ch.6], corresponding to a Cartan connection, i.e. a associated differential operator corresponding to a Cartan connection. We avoid these technicalities and use ‘‘Cartan connection’’ (a Koszul connection in [69]) and ‘‘Cartan-Ehresmann connection form’’ (Ehresmann connection in [69]).

The proof follows on the line of [39] and is given in [68]. As seen in the theorem above, we define the notion of covariant derivatives independent of the metric \mathcal{G} on $SIM(2)$, which is the underlying principle behind the Cartan connection. Although in principle these two entities need not be related, in Lemma 21 we show that the connection induced above is metric compatible.

Definition 20 Let (M, \mathcal{G}) be a Riemannian manifold (or pseudo-Riemannian manifold) where M and \mathcal{G} denote the manifold and the metric defined on it respectively. Let ∇ denote a connection on (M, \mathcal{G}) . Then ∇ is called metric compatible with respect to \mathcal{G} if

$$\nabla_Z \mathcal{G}(X, Y) = \mathcal{G}(\nabla_Z X, Y) + \mathcal{G}(X, \nabla_Z Y), \quad (89)$$

for all $X, Y, Z \in T(M)$.

Lemma 21 The Cartan connection D on $(SIM(2), T(SIM(2)))$ is metric compatible with respect to $\mathcal{G}_\beta : SIM(2) \times T(SIM(2)) \times T(SIM(2)) \rightarrow \mathbb{C}$ on $SIM(2)$ defined in (82).

Proof We first note that $D_{\mathcal{A}_i} \mathcal{G}(\mathcal{A}_j, \mathcal{A}_k) = 0$, $i \in \{1, 2, 3, 4\}$ as the covariant derivative of a scalar field is the same as partial derivative. Here $\{\mathcal{A}_i\}_{i=1}^4$ denote the basis of the left invariant vector fields $\mathcal{L}(SIM(2))$. The following brief computation

$$\mathcal{G}(D_{\mathcal{A}_i} \mathcal{A}_j, \mathcal{A}_k) + \mathcal{G}(\mathcal{A}_j, D_{\mathcal{A}_i} \mathcal{A}_k) = \mathcal{G}(c_{ij}^l \mathcal{A}_l, \mathcal{A}_k) + \mathcal{G}(\mathcal{A}_j, c_{ik}^m \mathcal{A}_m) = -c_{ij}^k - c_{ik}^j, \quad (90)$$

where we have used the fact that $\Gamma_{ij}^k = c_{ji}^k$ along with non-zero structure constants $c_{12}^3 = -c_{21}^3 = -c_{13}^2 = c_{31}^2 = -c_{34}^3 = c_{43}^3 = c_{42}^2 = -c_{24}^2 = 1$, leads to the result. \square

The next theorem relates the previous results on Cartan connections and covariant derivatives to the non-linear diffusion schemes on $SIM(2)$.

Theorem 22 covariant derivative of a co-vector field \mathbf{a} on the manifold $(SIM(2), \mathcal{G})$ is a $(0, 2)$ -tensor field with components $\nabla_j a_i = \mathcal{A}_j a_i - \Gamma_{ij}^k a_k$, whereas the covariant derivative of a vector field \mathbf{v} on $SIM(2)$ is a $(1, 1)$ -tensor field with components⁷ $\nabla_{j'} v^i = \mathcal{A}_{j'} v^i + \Gamma_{j'k'}^i v^{k'}$. The Christoffel symbols equal minus the structure constants of the Lie algebra $\mathcal{L}(SIM(2))$, i.e. $\Gamma_{ij}^k = -c_{ij}^k$. The Christoffel symbols are anti-symmetric as the underlying Cartan connection D has constant torsion. The left-invariant equations (42) with a diagonal diffusion tensor (44) can be rewritten in covariant derivatives as

$$\begin{cases} \partial_s W(g, s) = \sum_{i,j=1}^4 \mathcal{A}_i((D_{ij}(W))(g, s)) \mathcal{A}_j W(g, s) = \sum_{i,j=1}^4 \nabla_i((D_{ij}(W))(g, s)) \nabla_j W(g, s), \\ W(g, 0) = \mathcal{W}_\psi f(g), \text{ for all } g \in SIM(2), s > 0. \end{cases} \quad (91)$$

Both convection and diffusion in the left-invariant evolution equations (42) take place along the exponential curves in $SIM(2)$ which are covariantly constant curves with respect to the Cartan connection.

For proof see [68].

Remark 23 Though the connection D is \mathcal{G} compatible (Lemma 21), we have shown in the previous theorem that our connection is not torsion free, i.e. the torsion tensor $T(X, Y) \neq 0$ for all $X, Y \in T(SIM(2))$. As a result minimum distance curves in the group $SIM(2)$ are curves minimizing the induced Riemannian metric and do not coincide with “straight curves” (auto-parallel curves) in the group $SIM(2)$. The auto-parallel curves are the exponential curves. A full analysis of the shortest distance curves in $SIM(2)$ is beyond the scope of this article.

⁷We have made use of the notation $\nabla_j := D_{\mathcal{A}_j}$, when imposing the Cartan connection.

G Curvature estimation via best Exponential Curve fit

Curvature estimation of a spatial curve using $SE(2)$ -OS is based on the optimal exponential curve fit at each point. In [39, 7] the authors suggest two methods for such best exponential curve fit. Below is a brief summary.

- Compute the curvature of the projection $\mathbf{x}(s(t)) = \mathbb{P}_{\mathbb{R}^2}(g_0 \exp(t \sum_{i=1}^3 c_*^i A_i))$ of the optimal exponential curve in $SE(2)$ on the ground plane from an eigenvector $\mathbf{c}_* = (c_*^\theta, c_*^\xi, c_*^\eta)$. This eigenvector of $(\tilde{H}_\beta|U|)^T(\tilde{H}_\beta|U|)$, with a 3×3 Hessian

$$\tilde{H}_\beta|U| = \begin{pmatrix} \beta^2 \partial_\theta \partial_\theta |U| & \beta \partial_\xi \partial_\theta |U| & \beta \partial_\eta \partial_\theta |U| \\ \partial_\theta \partial_\xi |U| & \partial_\xi \partial_\xi |U| & \partial_\eta \partial_\xi |U| \\ \partial_\theta \partial_\eta |U| & \partial_\xi \partial_\eta |U| & \partial_\eta \partial_\eta |U| \end{pmatrix}, \quad (92)$$

corresponds to the smallest eigenvalue. The curvature estimation is given by,

$$\kappa_{est} = \|\ddot{x}(s)\| \operatorname{sgn}(\ddot{x}(s) \cdot \mathbf{e}_\eta) = \frac{c_*^\theta \operatorname{sign}(c_*^\xi)}{\sqrt{(c_*^\xi)^2 + (c_*^\eta)^2}}.$$

Note that unlike the $SIM(2)$ case curvature is constant in this case.

- In this method the choice of optimal exponential curve is restricted to horizontal exponential curves, which are curves in the $(SE(2), \omega^3)$ sub-Riemannian manifold. The idea is to diffuse along horizontal curves because typically the mass of a $SE(2)$ -OS is concentrated around a horizontal curve [7] and therefore this is a fast curvature estimation method.

Compute the curvature of the projection $\mathbf{x}(s(t)) = \mathbb{P}_{\mathbb{R}^2}(g_0 \exp(t \sum_{i=1}^3 c_*^i A_i))$ of the optimal exponential curve in $SE(2)$ on the ground plane from the eigenvector $\mathbf{c}_* = (c_*^\theta, c_*^\eta)$. This eigenvector of $(\tilde{H}_\beta^{hor}|U|)^T(\tilde{H}_\beta^{hor}|U|)$, with a 3×2 horizontal Hessian

$$\tilde{H}_\beta^{hor}|U| = \begin{pmatrix} \beta^2 \partial_\theta \partial_\theta |U| & \beta \partial_\xi \partial_\theta |U| \\ \partial_\theta \partial_\xi |U| & \partial_\xi \partial_\xi |U| \\ \partial_\theta \partial_\eta |U| & \partial_\xi \partial_\eta |U| \end{pmatrix}, \quad (93)$$

corresponds to the smallest eigenvalue. The curvature estimation given by,

$$\kappa_{est}^{hor} = \|\ddot{x}(s)\| \operatorname{sgn}(\ddot{x}(s) \cdot \mathbf{e}_\eta) = \frac{c_*^\theta}{c_*^\xi}.$$

For numerical experiments on these curvature estimates on orientation scores of noisy images, see [7].

References

References

- [1] T. Lindeberg, Scale-Space Theory in Computer Vision, Kluwer international series in engineering and computer science: Robotics: Vision, manipulation and sensors, Springer, 1993.
- [2] L. Alvarez, F. Guichard, P.-L. Lions, J.-M. Morel, Axioms and fundamental equations of image processing, Archive for rational mechanics and analysis 123 (3) (1993) 199–257.
- [3] B. ter Haar Romeny, L. Florack, J. Koenderink, M. Viergever, Scale-Space Theory in Computer Vision: First International Conference, Scale-Space'97, Utrecht, The Netherlands, July 2-4, 1997, Proceedings, Vol. 1252, Springer, 1997.
- [4] T. Lindeberg, Generalized axiomatic scale-space theory, in: Advances in Imaging and Electron Physics, Vol 178, Advances in Imaging and Electron Physics, Elsevier, 2013, pp. 1–96.

- [5] P. Perona, J. Malik, Scale-space and edge detection using anisotropic diffusion, *Pattern Analysis and Machine Intelligence*, IEEE Transactions on 12 (7) (1990) 629–639. doi:10.1109/34.56205.
- [6] J. Weickert, Coherence-enhancing diffusion filtering, *International Journal of Computer Vision* 31 (2-3) (1999) 111–127.
- [7] E. Franken, R. Duits, Crossing-preserving coherence-enhancing diffusion on invertible orientation scores, *International Journal of Computer Vision* 85 (2009) 253–278.
- [8] H. Scharr, K. Krajsek, A short introduction to diffusion-like methods, in: *Mathematical methods for signal and image analysis and representation*, Computational imaging and vision, Springer London, 2012, Ch. 1.
- [9] R. Duits, B. Burgeth, Scale spaces on lie groups, in: *Proceedings of the 1st international conference on Scale space and variational methods in computer vision*, SSVM’07, Springer-Verlag, Berlin, Heidelberg, 2007, pp. 300–312.
- [10] G. Citti, A. Sarti, A cortical based model of perceptual completion in the roto-translation space, *Journal of Mathematical Imaging and Vision* 24 (3) (2006) 307–326.
- [11] R. Duits, H. Führ, B. Janssen, M. Bruurmijn, L. Florack, H. van Assen, Evolution equations on gabor transforms and their applications, *Applied and Computational Harmonic Analysis* 35 (2013) 483–526.
- [12] R. Duits, Perceptual Organization in Image Analysis, Ph.D. thesis, Technische Universiteit Eindhoven (2005). URL <http://bmia.bmt.tue.nl/people/RDuits/THESISRDuits.pdf>
- [13] G. C. DeAngelis, I. Ohzawa, R. D. Freeman, Receptive-field dynamics in the central visual pathways, *Trends in Neurosciences* 18 (10) (1995) 451 – 458.
- [14] R. Young, The gaussian derivative model for spatial vision: I. retinal mechanisms, *Spatial Vision* 2 (4) (1987) 273–293.
- [15] M. Landy, J. Movshon, *Computational models of visual processing*, Bradford book, Mit Press, 1991.
- [16] W. Bosking, Y. Zhang, B. Schofield, D. Fitzpatrick, Orientation selectivity and the arrangement of horizontal connections in tree shrew striate cortex, *The Journal of Neuroscience* 17(6) (1997) 2112–2127.
- [17] R. Duits, M. Felsberg, G. Granlund, B. Romeny, Image analysis and reconstruction using a wavelet transform constructed from a reducible representation of the euclidean motion group, *Int. J. Comput. Vision* 72 (1) (2007) 79–102.
- [18] J.-P. Antoine, R. Murenzi, Two-dimensional directional wavelets and the scale-angle representation, *Signal Processing* 52 (3) (1996) 259 – 281.
- [19] J.-P. Antoine, R. Murenzi, P. Vandergheynsta, Directional wavelets revisited: Cauchy wavelets and symmetry detection in patterns, *Applied and Computational Harmonic Analysis* 6 (3) (1999) 314 – 345.
- [20] J.-P. Antoine, R. Murenzi, P. Vandergheynst, S. Ali, *Two-dimensional wavelets and their relatives*, Cambridge University Press, 2004.
- [21] L. Jacques, L. Duval, C. Chaux, G. Peyré, A panorama on multiscale geometric representations, intertwining spatial, directional and frequency selectivity, *Signal Processing* 91 (12) (2011) 2699–2730.
- [22] S. T. Ali, J.-P. Antoine, J.-P. Gazeau, *Coherent States, Wavelets, and Their Generalizations*, Springer New York, 2014.
- [23] D. Donoho, E. Candès, Ridgelets: a key to higher-dimensional intermittency?, *Royal Society of London Philosophical Transactions Series A* 357 (1999) 2495.
- [24] D. Donoho, E. Candès, Continuous curvelet transform: I. resolution of the wavefront set, *Applied and Computational Harmonic Analysis* 19 (2) (2005) 162 – 197.
- [25] D. Donoho, E. Candès, Continuous curvelet transform: II. discretization and frames, *Applied and Computational Harmonic Analysis* 19 (2) (2005) 198 – 222.
- [26] E. Candès, L. Demanet, D. Donoho, L. Ying, Fast discrete curvelet transforms, *Multiscale Modeling and Simulation* 5 (2006) 861–899.
- [27] D. Labate, W.-Q. Lim, G. Kutyniok, G. Weiss, Sparse multidimensional representation using shearlets, in: *Optics & Photonics 2005*, International Society for Optics and Photonics, 2005, pp. 59140U–59140U.
- [28] K. Guo, D. Labate, Optimally sparse multidimensional representation using shearlets, *SIAM journal on mathematical analysis* 39 (1) (2007) 298–318.

- [29] S. Dahlke, G. Steidl, G. Teschke, Shearlet coorbit spaces: compactly supported analyzing shearlets, traces and embeddings, *Journal of Fourier Analysis and Applications* 17 (6) (2011) 1232–1255.
- [30] B. G. Bodmann, G. Kutyniok, X. Zhuang, Gabor shearlets, *arXiv preprint (arXiv:1303.6556)* (2013).
- [31] S. T. Ali, A general theorem on square-integrability: Vector coherent states, *J. Math. Phys.* 39(8) (1998) 3954–3964.
- [32] D. H. Hubel, Evolution of ideas on the primary visual cortex, 1955-1978: A biased historical account, *Physiology or Medicine Literature Peace Economic Sciences, Nobel Prize Lectures* (1993) 24.
- [33] A. Grossmann, J. Morlet, T. Paul, Transforms associated to square integrable group representations. I. General results, *J. Math. Phys.* 26 (10) (1985) 2473–2479.
- [34] H. Führ, *Abstract Harmonic Analysis of Continuous Wavelet Transforms*, no. 1863 in *Lecture Notes in Mathematics*, Springer, 2005.
- [35] S. Kalitzin, B. Romeny, M. Viergever, Invertible apertured orientation filters in image analysis, *International Journal of Computer Vision* 31 (2-3) (1999) 145–158.
- [36] E. Bekkers, R. Duits, T. Berendschot, B. ter Haar Romeny, A multi-orientation analysis approach to retinal vessel tracking, *Journal of Mathematical Imaging and Vision* (2012) 1–28.
- [37] R. Duits, M. Almsick, The explicit solutions of linear left-invariant second order stochastic evolution equations on the 2D Euclidean motion group, *Quarterly of Applied Mathematics* 66 (2008) 27–67.
- [38] R. Duits, E. Franken, Left-invariant parabolic evolutions on $SE(2)$ and contour enhancement via invertible orientation scores part I: Linear left-invariant diffusion equations on $SE(2)$, *Quarterly of Applied Mathematics* 68 (2010) 255–292.
- [39] R. Duits, E. Franken, Left-invariant parabolic evolutions on $SE(2)$ and contour enhancement via invertible orientation scores part II: Nonlinear left-invariant diffusions on invertible orientation scores, *Quarterly of Applied Mathematics* 68 (2010) 293–331.
- [40] F. Martens, Spaces of analytic functions on inductive/projective limits of Hilbert Spaces, Ph.D. thesis, Technische Universiteit Eindhoven (1988).
URL <http://alexandria.tue.nl/extra3/proefschrift/PRF6A/8810117.pdf>
- [41] A. Borel, H. Bass, *Linear algebraic groups*, Vol. 126, Springer-Verlag New York, 1991.
- [42] U. Boscaïn, J.-P. Gauthier, R. Chertovskih, A. Remizov, Hypocoelliptic diffusion and human vision, *arXiv preprint (arXiv:1304.2062)* (2013).
- [43] I. Bankman, *Handbook of Medical Image Processing and Analysis*, Academic Press Series in Biomedical Engineering, Elsevier/Academic Press, 2008.
- [44] J. Zhang, H. Huang, Automatic background recognition and removal (abbr) in computed radiography images, *Medical Imaging, IEEE Transactions on* 16 (6) (1997) 762–771. doi:10.1109/42.650873.
- [45] L. Jacques, J.-P. Antoine, Multiselective pyramidal decomposition of images: wavelets with adaptive angular selectivity, *International Journal of Wavelets, Multiresolution and Information Processing* 5 (05) (2007) 785–814.
- [46] M. Unser, Splines: A perfect fit for signal/image processing, *IEEE Signal Processing Magazine* 16 (1999) 22–38.
- [47] J. Dieudonné, *Treatise on Analysis*, no. v. 5 in *Pure and applied mathematics*, Academic Press, 1977.
- [48] T. Aubin, *A course in differential geometry*, Graduate studies in mathematics, American Mathematical Society, 2001.
- [49] L. Hörmander, Hypocoelliptic second order differential equations, *Acta Mathematica* 119 (1967) 147–171.
- [50] R. Duits, E. Franken, Left-invariant diffusions on the space of positions and orientations and their application to crossing-preserving smoothing of hardi images, *Int. J. Comput. Vision* 92 (3) (2011) 231–264.
- [51] E. Hsu, *Stochastic analysis on manifolds*, Contemporary Mathematics, American Mathematical Society, 2002.
- [52] A. Nagel, F. Ricci, E. M. Stein, Fundamental solutions and harmonic analysis on nilpotent groups, *Bulletin of American Mathematical Society* 23 (1990) 139–144.
- [53] A. ter Elst, D. Robinson, Weighted subcoercive operators on Lie groups, *Journal of Functional Analysis* 157 (1) (1998) 88 – 163.

- [54] S. Mallat, Group invariant scattering, *Communications on Pure and Applied Mathematics* 65 (10) (2012) 1331–1398.
- [55] L. Sifre, S. Mallat, E. N. S. DI, Rotation, scaling and deformation invariant scattering for texture discrimination, in: *Proc. CVPR*, 2013.
- [56] E. Franken, Enhancement of crossing elongated structures in images, Ph.D. thesis, Technische Universiteit Eindhoven (2008).
URL <http://alexandria.tue.nl/extra2/200910002.pdf>
- [57] N. Patton, T. M. Aslam, T. MacGillivray, I. J. Deary, B. Dhillon, R. H. Eikelboom, K. Yogesan, I. J. Constable, Retinal image analysis: concepts, applications and potential, *Progress in retinal and eye research* 25 (1) (2006) 99–127.
- [58] A. Budai, J. Hornegger, G. Michelson, Multiscale approach for blood vessel segmentation on retinal fundus images, *Investigative Ophthalmology and Visual Science* 50 (5) (2009) 325.
- [59] M. D. Abramoff, M. K. Garvin, M. Sonka, Retinal imaging and image analysis, *Biomedical Engineering, IEEE Reviews in* 3 (2010) 169–208.
- [60] X. Xu, M. Niemeijer, Q. Song, M. Sonka, M. K. Garvin, J. M. Reinhardt, M. D. Abramoff, Vessel boundary delineation on fundus images using graph-based approach, *Medical Imaging, IEEE Transactions on* 30 (6) (2011) 1184–1191.
- [61] P. Bankhead, C. N. Scholfield, J. G. McGeown, T. M. Curtis, Fast retinal vessel detection and measurement using wavelets and edge location refinement, *PloS one* 7 (3) (2012) e32435.
- [62] A. F. Frangi, W. J. Niessen, K. L. Vincken, M. A. Viergever, Multiscale vessel enhancement filtering, in: *Medical Image Computing and Computer-Assisted Intervention MICCAI’98*, Springer, 1998, pp. 130–137.
- [63] J. Hannink, R. Duits, E. Bekkers, Vesselness via multiple scale orientation scores, *arXiv preprint* (2014).
URL <http://arxiv.org/abs/1402.4963>
- [64] H. J. Seo, P. Chatterjee, H. Takeda, P. Milanfar, A comparison of some state of the art image denoising methods, in: *Signals, Systems and Computers, 2007. ACSSC 2007. Conference Record of the Forty-First Asilomar Conference on*, IEEE, 2007, pp. 518–522.
- [65] A. Buades, B. Coll, J.-M. Morel, A review of image denoising algorithms, with a new one, *Multiscale Modeling & Simulation* 4 (2) (2005) 490–530.
- [66] H. Takeda, S. Farsiu, P. Milanfar, Kernel regression for image processing and reconstruction, *Image Processing, IEEE Transactions on* 16 (2) (2007) 349–366.
- [67] M. Rubbens, A. Mol, R. Boerboom, R. Bank, F. Baaijens, C. Bouten, Intermittent straining accelerates the development of tissue properties in engineered heart valve tissue, *Tissue Engineering: Part A* 15 (5).
- [68] U. Sharma, R. Duits, Left-invariant evolutions of wavelet transforms on the similitude group, *CASA Report* 13-17, Technische Universiteit Eindhoven (June 2013).
URL <http://www.win.tue.nl/analysis/reports/rana13-17.pdf>
- [69] M. Spivak, *A Comprehensive Introduction to Differential Geometry, Vol-II*, 3rd ed., Publish or Perish Inc., 1970.